Lithospheric transdimensional ambient-noise tomography of W-Europe: implications for crustal-scale geometry of the W-Alps

Ahmed Nouibat, Laurent Stehly, Anne Paul, Stéphane Schwartz, Thomas Bodin, Thierry Dumont, Yann Rolland, Romain Brossier

submitted to *Geophys. J. Int.*

Lithospheric transdimensional ambient-noise tomography of W-Europe: implications for crustal-scale geometry of the W-Alps

A. Nouibat[1⋆], L. Stehly[1], A. Paul[1], S. Schwartz[1], T. Bodin[2], T. Dumont[1], Y. Rolland[1,3], R. Brossier[1], Cifalps Team and AlpArray Working Group[†]

[1] *Univ. Grenoble Alpes, Univ. Savoie Mont Blanc, CNRS, IRD, UGE, ISTerre, 38000 Grenoble, France.*

[2] *Univ. Lyon, UCBL, CNRS, LGL-TPE, 69622 Villeurbanne, France.*

[3] *Univ. Savoie Mont Blanc, CNRS, UMR 5204, EDYTEM, 73370 Le Bourget-du-Lac, France.*

SUMMARY

A full understanding of the dynamics of mountain ranges such as the Alps requires the integration of available geological and geophysical knowledge into a lithospheric-scale three-dimensional geological model. As a first stage in the construction of this geo-model, we derive a new 3-D shear-wave velocity model of the Alpine region, with a spatial resolution of a few tens of kilometers, making it possible to compare with geological maps. We use four years of continuous vertical-component seismic noise records to compute noise correlations between more than 950 permanent broadband stations complemented by ~ 600 temporary stations from the AlpArray sea-land seismic network and the Cifalps and EASI linear arrays. A specific pre-processing is applied to records of ocean-bottom seismometers in the Liguro-Provençal basin to clean them from instrumental and oceanic noises. We first perform a 2-D transdimensional inversion of the travel times of Rayleigh waves to compute group-velocity maps from 4 to 150 s. The data noise level treated as an unknown parameter is determined with a Hierarchical Bayes method. A Fast Marching

Eikonal solver is used to update raypath geometries during the inversion. We use next the group-velocity maps and their uncertainties to derive a 3-D probabilistic V_s model. The probability distributions of V_s at depth and the probability of presence of an interface are estimated at each location by exploring a set of 130 million synthetic four-layer 1-D V_s models. The obtained probabilistic model is refined using a linearized inversion. Throughout the inversion for V_s, we include the water column where necessary. Our V_s model highlights strong along-strike changes of the lithospheric structure, particularly in the subduction complex between the European and Adriatic plates. In the South-Western Alps, our model confirms the existence of a low-velocity structure at $50 - 80$ km depth in the continuation of the European continental crust beneath the subduction wedge. This deep low-velocity anomaly progressively disappears towards the North-Western and Central Alps. The European crust includes lower crustal low-velocity zones and a Moho jump of $\sim 8 - 12$ km beneath the western boundary of the External Crystalline Massifs of the North-Western Alps. The striking fit between our V_s model and the receiver function migrated depth section along the Cifalps profile documents the reliability of the V_s model. In light of this reliability and with the aim to building a 3-D geological model, we re-examine the geological structures highlighted along the Cifalps profile.

Key words: Seismic tomography, Surface waves and free oscillations, Seismic noise, Crustal structure, Europe

1 INTRODUCTION

Since the Late Cretaceous, the geodynamic evolution of Western Europe has been dominated by convergence between the European and African plates. This long-term motion resulted in the formation of the Alps and other peri-Mediterranean mountain ranges (Pyrenees, Dinarides, Apennines, Carpathians, etc.) and also caused the opening of the Western European Cenozoic Rift System and of Mediterranean back-arc oceanic domains (Fig. 1a) (Faccenna et al., 2014). In the Alps, convergence resulted in oceanic subduction from Late Cretaceous to Early Eocene (e.g., Handy et al., 2010), later on followed

⋆ E-mail : ahmed.nouibat@univ-grenoble-alpes.fr
† AlpArray Working Group (http://www.alparray.ethz.ch/home/)

by continental subduction of the European margin (e.g., Chopin, 1984; Duchêne et al., 1997; Guillot et al., 2009; Zhao et al., 2015). From Oligocene onwards, continental collision resulted in thrusting of the subduction wedge towards the European foreland, marked by the development of the Penninic Frontal Thrust (PFT) (Simon-Labric et al., 2009).

The objective of this study is to improve the resolution of seismic models of the lithospheric structure of Western Europe in order to better constrain 3-D geological structures, particularly in the Alpine mountain belt and its forelands. For this, we build a new 3-D high-resolution shear-wave velocity model using ambient-noise records of an exceptional array of seismic stations (Fig. 1b). To assess the robustness and the geological significance of our 3-D V_s model, we focus its geological interpretation on the Western Alps where the near-surface geology is well-documented and a number of high-resolution geophysical investigations have been carried out recently (see review in Malusà et al., 2021).

In the internal zones of the Western Alps, the continental subduction of the European crust beneath the Adriatic lithosphere was first highlighted by the observation of preserved UHP minerals (e.g. coesite) in the outcropping subduction wedge (Chopin, 1984). Recently, receiver functions of the Cifalps experiment have imaged the continuity of the subducted European continental crust down to $75 - 80\ km$ depth (Zhao et al., 2015). In this context, the combination of tectonics, petrophysics and numerical thermodynamics has provided conceptual models that are consistent with the formation of a subduction wedge during plate convergence (Burov et al., 2014; Liao et al., 2018), and with the involvement of serpentinites in the burial/exhumation processes (Schwartz et al., 2001; Guillot et al., 2009). However, despite the geological structure of the Western Alps having been studied for more than a century, correlating geological units mapped at the surface with geophysical images of the crust remains challenging. This is due to the limited resolution of these images, the lack of accurate uncertainty estimates, and the non-unicity of their geological interpretations regarding lithology, thermicity, fluids and deformation. Moreover, some first order questions remain controversial, such as the nature of the geophysical Ivrea body (e.g., Schmid et al., 2017; Solarino et al., 2018), and the precise geometry of the Adria mantle wedge and its role in the partitioning of the present-day strain field (Lardeaux et al., 2006; Eva et al., 2020).

Since the 1990's, the structure of the lithosphere beneath the Western Alps has been probed by a broad spectrum of geophysical techniques. The ECORS-CROP normal-incidence and wide-angle reflection controlled-source seismic survey (CSS) has provided a very high-resolution image of the reflectivity of the crust in the North-Western Alps (Nicolas et al., 1990). Local earthquake tomography (LET) studies have yielded local or regional 3-D P-wave velocity models of the crust (e.g., Paul et al., 2001; Diehl et al., 2009; Solarino et al., 2018). Receiver functions (*RF*) have been used to map Moho

depth as a complement to the 2-D CSS profiles and 3-D LET models (e.g., Spada et al., 2013; Zhao et al., 2015). These geophysical data have lower resolution than surface geological data. They were however of great help to constrain to the first order the 3-D geometry of the crustal structure under the Western Alps. In particular, they highlighted the underthrusting of the European plate beneath the Adria micro-plate, with a maximum Moho depth locally reaching $55\ km$ (ECORS-CROP Deep Seismic Sounding Group, 1989; Thouvenot et al., 2007).

In the last decade, seismic imaging of the Alpine lithosphere has improved thanks to the densification of permanent broadband seismological networks and the multiplication of temporary experiments (e.g., Cifalps-2, Liu et al., 2022; AlpArray, Hetényi et al., 2018a). New passive imaging methods have been introduced that make optimal use of these dense station arrays and are independent of earthquake or active source illumination. Paul & Campillo (2003) and Shapiro & Campillo (2004) have shown that the cross-correlation of long time series of diffuse wavefields including ambient noise recorded at two seismic stations leads to the reconstruction of the surface waves propagating between the two stations as if a virtual seismic source is placed at one station with the emitted signal being recorded at the second station. Shapiro et al. (2005) have further shown that ambient-noise tomography (ANT) from continuous noise recordings over dense networks provides high resolution images of the crust and upper mantle. Since then, several S-wave velocity models have been derived from ANT to probe the crustal structure under the Alpine arc (e.g., Stehly et al., 2009; Verbeke et al., 2012; Molinari et al., 2015).

Taking advantage of the ever-increasing amount of available data, Kästle et al. (2018) used a stochastic inversion of travel times of surface waves from noise correlations, regional and teleseismic earthquakes to construct a 3-D V_s model of the entire Alpine region. Lu et al. (2018) used ambient-noise records of 1293 broadband stations, including the first six months of the AlpArray network, to derive a high-resolution 3-D V_s model of the European crust from ANT using a Bayesian inversion. This model was further refined in the Alpine region by Lu et al. (2020) using wave equation tomography (WET) of Rayleigh-wave phase dispersion data derived from noise correlations. Zhao et al. (2020) used Bayesian transdimensional inversion of the group-velocity dataset of Lu et al. (2020) to derive a shear-wave velocity model of the Western Alps that provides a particularly well-resolved image of the subduction. These new approaches highlighted major intra-crustal units confirmed by field observations, such as the subduction complex in the internal zone of the Alps, which is either located beneath a mantle wedge in the Western Alps or covered by Adriatic crustal units in the Central and Eastern Alps. Since the works by Lu et al. (2018, 2020) and Zhao et al. (2020), more data have been recorded, in particular in the Western Alps, that should contribute to improving the resolution of ambient-noise tomography.

In the present work, we generate a new 3-D shear-wave velocity model of Western Europe by combining ambient-noise tomography with probabilistic inversion. We use four years of continuous seismic noise records at all available broadband seismic stations including permanent networks, the Cifalps and Cifalps-2 profiles and the AlpArray network (see Fig. 1a, and section 2). We also include data of the AlpArray ocean-bottom seismometers to image the transition between the Ligurian sea and the Alpine region. This dataset gives a unique opportunity to image the crust and upper mantle below the Alpine belt and its forelands at an unprecedented resolution. The originality of our approach lies in the use of a transdimensional inversion to compute 2-D group-velocity maps and their uncertainties, which are then used to obtain a 3-D probabilistic shear-wave velocity model from a Bayesian inversion (sections 3 and 4). This model provides a probability distribution of V_s as well as the probability of presence of an interface at each depth and location. This approach was chosen specifically to image sharp lateral discontinuities, which is crucial in the Western Alps. To the best of our knowledge, this is the first time that a fully probabilistic approach is used at this scale to image the lithosphere. In section 5, we further assess the model robustness along the Cifalps profile (South-Western Alps) by comparing our results with a receiver-function depth section. Finally, we propose an updated crustal-scale interpretative geological cross-section based on previous geophysical-geological works (reviewed in Malusà et al., 2021), on our V_s model and the receiver-function section along the Cifalps profile. This comparison illustrates the potential contribution of our V_s model to the development of a 3-D geological model of the Alpine chain and its forelands.

2 AMBIENT-NOISE DATASET

2.1 Station coverage

Our dataset consists of four years of vertical-component, daily seismic noise records (2015-2019) of more than 950 permanent broadband seismic stations located in and around the Greater Alpine region, complemented by 490 temporary stations from the AlpArray (Z3 network, AlpArray Seismic Network, 2015), Cifalps (YP network, Zhao et al., 2016, and XT network, Zhao et al., 2018) and EASI experiments (XT network, AlpArray seismic network, 2014) (Fig. 1b). The average inter-station distance is $\sim 50\ km$ in the Greater Alpine region.

The on-land component of the AlpArray seismic network was operated for 2 to 4 years and covered the Greater Alpine area (Hetényi et al., 2018a). We also used data from 23 broadband ocean-bottom seismometers (OBS) that were deployed during $8-10$ months ($2017-2018$) in the Ligurian Sea as part of the AlpArray Seismic Network (AASN) (Hetényi et al., 2018a). The OBS component of the AASN was operated within the framework of a French-German cooperation that aimed at imaging the

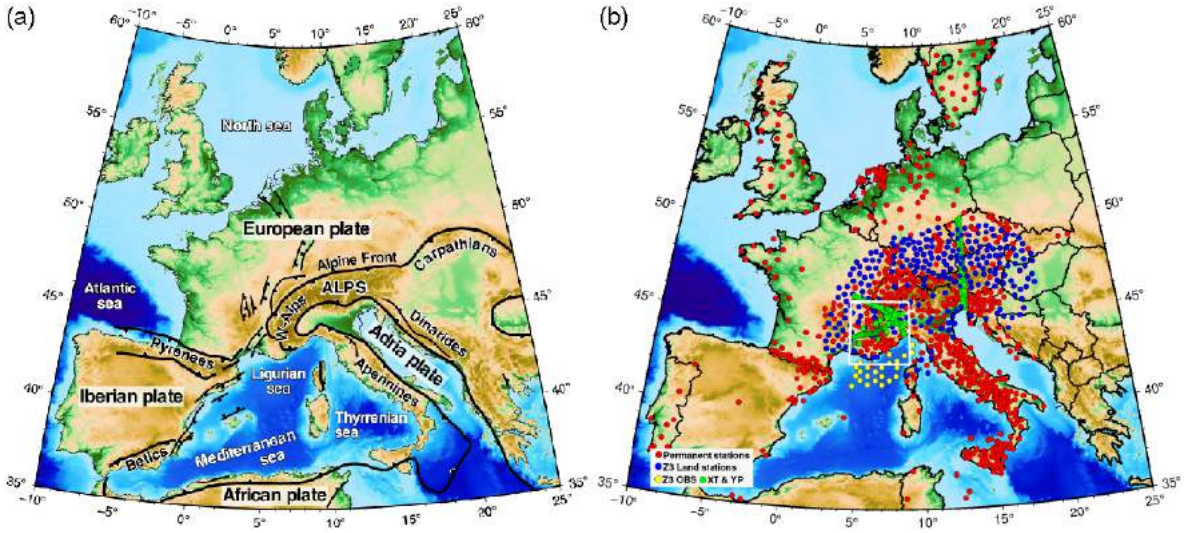

Figure 1. (a) Topographic map showing the regions, plates and main geological boundaries discussed in the text (modified from Faccenna et al., 2014). Black lines with triangles correspond to main thrusts and subduction zones. Black lines with squares represent extensional faults associated with development of the Western European Cenozoic Rift System. (b) Location map of the broadband seismic networks used in this study. The white frame which includes most of the Western Alps indicates the main focus area of this work.

lithospheric structure of the Ligurian basin and the transition between the Alps and the Apennines. OBS records are merged into the Z3 dataset, which means that data and metadata are archived in the same standard (FDSN) format as data recorded by on-land stations, and they are distributed by the RESIF and GEOFON nodes of the European Integrated Data Archive (EIDA) using the same procedures as on-land data. This integration of data recorded at sea-bottom and on land greatly facilitates their use in massive data processing such as that presented here.

In addition to the AASN, we also used data of the dense ($7 - 10\ km$ spacing) Cifalps (China-Italy-France Alps seismic survey) and Cifalps-2 linear arrays that operated for $14 - 15$ months in the Western Alps in $2012 - 2013$ and $2018 - 2019$, respectively. They provide a very dense coverage of the Western Alps, which are the main focus of this work (Fig. 1b).

2.2 Data processing and correlation

Before computing the correlations for each station pair, we pre-processed the noise records in two main steps. First, we applied a generic pre-processing scheme where each daily record was band-pass filtered between $2.5\ s$ and $300\ s$, corrected for the instrumental response, decimated to $1\ Hz$ sampling frequency and split into 4-hrs segments. Second, we decreased the contribution of earthquakes and other transient signals by (1) removing signals with amplitude 4 times greater than the standard deviation and (2) removing segments with RMS greater than 1.5 times the daily mean RMS (Boué

et al., 2014). Then, each daily record was filtered into several period bands ($3-5$, $5-10$, $10-20$, $20-40$, $40-80$ and $80-200$ seconds) and normalized by its envelope. Finally, the six filtered and normalized signals were stacked. We thus obtained a broadband signal with amplitude normalized in several period bands. This processing is similar to the one used by Soergel et al. (2019).

In addition, we used a specific processing for the data of the 23 OBS in order to reduce the tilt and the compliance effects using frequency-dependent response functions (Crawford & Webb, 2000). We also corrected the records of 8 OBS that were affected by periodic glitches of electronic origin. This was achieved using a template matching algorithm (Deen et al., 2017).

For each of the 1.1 million station pairs, we computed the cross-correlations of up to 4 years of vertical component continuous noise records by segments of 4 hours. The resulting cross-correlations were then normalized and stacked. Supplementary Fig. S1 shows distance-time sections of cross-correlations in the $5-10\ s$, $10-20\ s$ and $20-40\ s$ period bands. We used a specific computation scheme for correlations between ocean-bottom stations in order to enhance the signal-to-noise ratio. It was indeed poorer for OBS pairs than for on-land station pairs or mixed pairs of on-land and ocean-bottom stations. We took advantage of the large number of on-land stations and their high quality by using them as virtual sources for the OBS-OBS correlations. For each OBS pair, we correlated the ballistic Rayleigh waves of the noise correlations between each OBS and a large number of selected on-land stations, and stacked them to obtain the OBS-OBS correlation. This process is known as "C2" (for correlation of correlation) which is a variant that uses the ballistic waves rather than the coda (Stehly et al., 2008). Another publication will be dedicated to the processing of OBS records.

2.3 Group-velocity measurements

Once cross-correlations were computed for the entire dataset, we derived, for each pair of stations, the group-velocity dispersion curves of positive and negative correlation times by using multiple filter analysis (*MFA*, Dziewonski et al., 1969; Herrmann, 1973). Similarly to Lu et al. (2018), we adapted the width of the filter to the inter-station distance to accommodate the trade-off in resolution between the time and frequency domains (Levshin et al., 1989). We also corrected our group-velocity measurements for the systematic error that occurs with the *MFA* technique due to the strong amplitude decrease of the noise spectrum at periods $> 20\ s$ (Shapiro & Singh, 1999).

Careful selection of group-velocity measurements prior to group-velocity tomography is essential to prevent biases induced by the heterogeneous distribution of noise sources, by interferences of Rayleigh waves in the causal and acausal times and by instrumental problems. To that aim, for each station pair and period, we selected the group-velocity measurements with a signal-to-noise ratio > 3 and the group-velocity difference between causal and acausal Rayleigh waves $< 0.2\ km/s$. Further-

more, we only kept paths with length of 2 to 40 wavelengths at each period. By combining these criteria, we keep only the reliable travel time measurements for the subsequent 2-D group-velocity maps.

3 INVERSION FOR 2-D GROUP-VELOCITY MAPS

Our aim is to derive a 3-D probabilistic V_s model of the Alpine crust and upper mantle. As a first step towards this goal, we compute 2-D group-velocity maps and associated uncertainties using a transdimensional algorithm at discrete periods from $4\ s$ to $150\ s$.

Probabilistic group-velocity maps are derived by exploring millions of 2-D models with different parameterizations using the reversible-jump Markov-chain Monte-Carlo method (*rj-McMC*), first applied in a seismic tomography context by Bodin et al. (2012). The parameterization of the model is treated as part of the inversion without any explicit regularization. This allows the local resolution to self-adapt to the path density and to the variability of the information contained in group-velocity measurements. The model complexity required to fit the data is controlled by the noise level, which is treated as an extra parameter of the inversion and determined within a hierarchical Bayes formalism (Malinverno & Brigg, 2004).

Moreover, since the Alpine crust is strongly heterogeneous and displays sharp group-velocity contrasts, the non-linearity of the forward problem is accounted for by iteratively updating the raypath geometry using the fast marching method (*FMM*, Rawlinson & Sambridge, 2004). Ray bending is more sensitive to phase-velocity changes than to group-velocity changes. However, accounting for ray bending in group-velocity *rj-McMC* tomography has proven to be substantially more accurate in a heterogeneous medium than the straight ray assumption (e.g., Galetti et al., 2015).

3.1 Method

The 2-D velocity field is parameterized with a set of Voronoi cells with variable number and geometries. The velocity field is described by a vector of model parameters $\mathbf{m}$ giving the position and group velocity associated with each Voronoi cell.

The inverse problem is treated in a Bayesian framework, where the solution is represented by the posterior probability density function representing the probability of the model $\mathbf{m}$, given a set of observed data $\mathbf{d}$. The posterior solution is expressed according to Bayes's theorem (Bodin et al., 2012)

$$p(\mathbf{m}|\mathbf{d}) \propto p(\mathbf{d}|\mathbf{m})p(\mathbf{m}) \tag{1}$$

where $p(\mathbf{m})$ is the *a priori* probability density of the model parameters $\mathbf{m}$, i.e. what we know about the

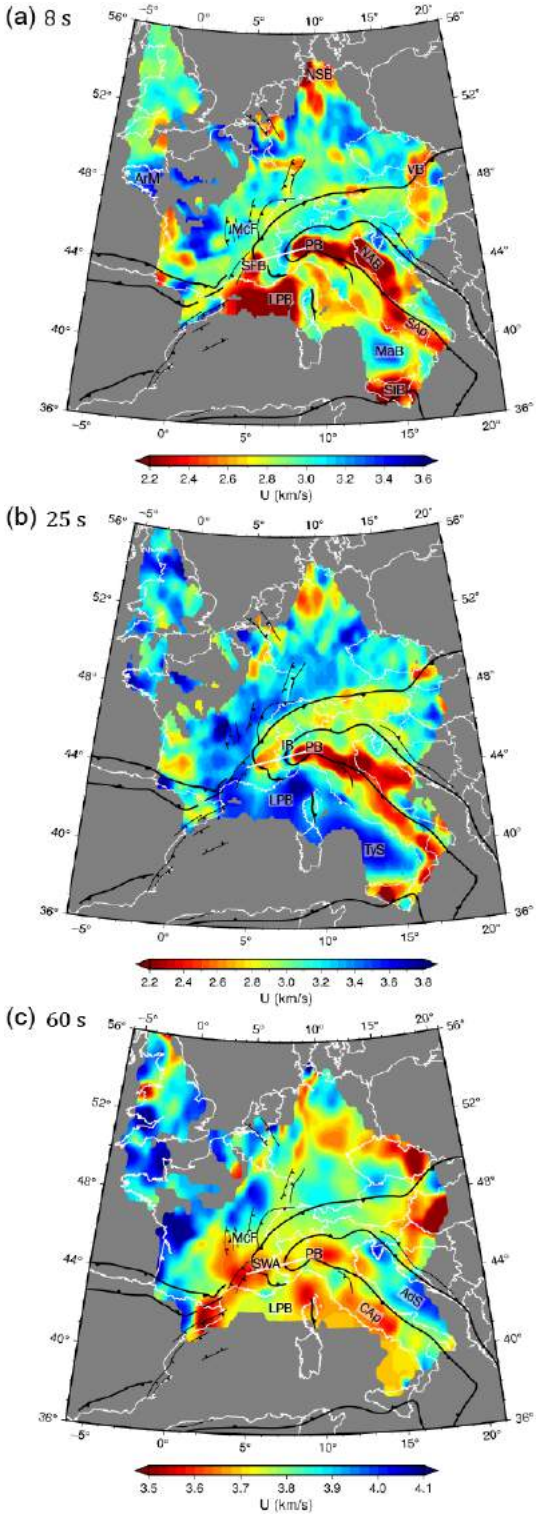

Figure 2. Group-velocity maps (average solutions) at (a) 8 s, (b) 25 s and (c) 60 s periods, obtained with the Hierarchical Bayes reversible-jump algorithm. Only areas with uncertainty lower than 0.5 km/s are shown. Black lines show the main geological boundaries as defined in Fig. 1a. The white line shows the Cifalps profile discussed in section 5. ArM: Armorican Massif, IB: Ivrea geophysical body, LPB: Liguro-Provençal basin, MaB: Marsili back-arc basin, McF: Eastern Massif Central, NAB: North-Adriatic basin, NSB: North-Sea basin, PB: Po basin, CAp: Central Apennines, SAp: Southern Apennines, SWA: South-Western Alps, SFB: Southeast-France basin, SiB: Sicily fold-and-thrust belt, TyS: Tyrrhenian Sea, VB: Vienna basin, AdS: Adriatic Sea.

velocity field independently of the data. The term $p(\mathbf{d}|\mathbf{m})$ is the likelihood function and represents the probability of observing $\mathbf{d}$ given a model $\mathbf{m}$, and given the statistics of data errors. Assuming normally distributed uncorrelated data errors, $p(\mathbf{d}|\mathbf{m})$ can be expressed with the general Gaussian form

$$p(\mathbf{d}|\mathbf{m}) = \frac{1}{\prod_{i=1}^{N} \sqrt{2\pi}\sigma_{d_i}} \times \exp\left(\frac{-\phi(\mathbf{m})}{2}\right) \tag{2}$$

where σ_{d_i} is the standard deviation of data errors on the ith observation, N is the number of observations, and $\phi(\mathbf{m})$ is the misfit function for the model $\mathbf{m}$

$$\phi(\mathbf{m}) = \sum_{i=1}^{N} \left[\frac{(g(\mathbf{m}) - \mathbf{d})^2}{\boldsymbol{\sigma}_{\boldsymbol{d}}^2}\right]_i \tag{3}$$

The term $g_i(\mathbf{m})$ represents data computed by the forward problem, i.e. the travel time of the ith ray predicted by the model $\mathbf{m}$, and computed from

$$g_i(\mathbf{m}) = \sum_{j=1}^{n} \frac{L_{ij}}{v_j} \tag{4}$$

where L_{ij} is the length of the ith ray across the Voronoi cell j of velocity v_j.

The posterior probability distribution can be estimated with the reversible-jump *McMC* algorithm, which produces a large ensemble of models, whose distribution approximates the posterior solution. The algorithm is based on a Markov-chain Monte-Carlo sampler where at each iteration, a new velocity model is proposed by perturbing the current model (e.g. perturb the geometry of the Voronoi discretization, change the velocity within one Voronoi cell). The proposed model is then either accepted or rejected in the ensemble depending on an acceptance criteria based on the ratio of posterior values of the current and proposed model. Once the algorithm has been run for enough iterations, statistics can be extracted from the ensemble solution for interpretation. For example, at any geographical location, the mean and standard deviation of velocities can be used to produce a group-velocity map, with associated error estimates. We refer the reader to Bodin et al. (2012), for more details.

3.2 2-D group-velocity maps

We performed the *rj-McMC* tomography to derive group-velocity maps for periods between $4\ s$ and $150\ s$. For each period, 64 Markov chains were run in parallel to explore independently the model space. Each individual process was run for 180×10^3 steps in total. Once the convergence was achieved, the ensemble of sampled models was averaged to produce a smooth average solution, that can be interpreted as the mean of the posterior solution. We used this average model to update ray path geometry and recalculate traveltimes using the *FMM*. The global scheme was run for 2 iterations, resulting in the group-velocity maps shown in Figures 2 and 3.

At 8 s period (mainly sensitive to $\sim 5-8$ km depth; Fig. 2a), the clearest features of the group-velocity map are low-velocity anomalies associated with thick sedimentary basins: the Po basin (labeled PB in Fig. 2a) and the North-Adriatic basin (NAB), the Liguro-Provençal basin (LPB), the Southeast-France basin (SFB), the Vienna basin (VB) in the easternmost part of our study area and part of the North-Sea basin in Northern Germany (NSB). The Southern Apennines (SAp) and the Sicily fold-and-thrust belt (SiB) are also characterized by low velocities. The highest velocities (> 3.2 km/s) are observed in the Variscan massifs of France such as the Western Massif Central (McF) and the Armorican Massif (ArM), and in the Marsili back-arc basin (MaB) of the Tyrrhenian Sea. Supplementary Fig. S2a shows the main sedimentary basins on the 8-s group-velocity map.

At 25 s (sensitive to $\sim 15-30$ km depth; Fig. 2b), the Liguro-Provençal basin (LPB in Fig. 2b) has velocities > 3.5 km/s due to the thin crust of the basin. Similar high-velocity anomalies are observed in the Tyrrhenian Sea (TyS) and to the west and north of the Alpine front in the Western and Central Alps. The very thick Po basin (PB) is still characterized by very low velocities (< 2.3 km/s), while slightly higher velocities ($\sim 2.5-2.6$ km/s) prevail in the Apenninic belt and moderately low velocities ($\sim 2.7-3.0$ km/s) in the Alpine belt. The strong high-velocity anomaly associated with the shallow mantle flake known as the Ivrea geophysical body is observed between the Po basin and the Western Alps (IB in Fig. 2b) in spite of its small size ($\sim 10-15$ km width). This gives a first insight into the good lateral resolution of our 2-D tomography. Supplementary Fig. S2b shows the comparison between the 25-s map and the reference Moho depth model of Spada et al. (2013).

At 60 s (sensitive to $\sim 50-100$ km depth; Fig. 2c), the upper mantle appears as heterogeneous as for shorter periods with low-velocity anomalies beneath the Po basin (PB) and the central Apennines (CAp), the Liguro-Provençal basin (LPB), the south of the French Massif Central (McF) and the South-Western Alps (SWA). High-velocity anomalies are observed beneath the Adriatic Sea (AdS) and in the northwest of the model.

3.3 Uncertainty estimates

At each geographical location i, we extracted posterior uncertainties from the variance of the ensemble of sampled velocities. This uncertainty is given by

$$\sigma_i = \sqrt{\frac{1}{M}\sum_{j=1}^{M}\Big(v(m_j)-\overline{v}\Big)_i^2} \tag{5}$$

where M is the total number of models in the Markov-chain ensemble and $\overline{v}$ the average solution model. This uncertainty is primarily related to the complexity of the velocity structure, but also depends on the reliability of the observations and on raypath coverage.

The uncertainty map displayed in Fig. 3b for 15 s period shows that our group-velocity model (Fig. 3a) is better constrained in the Greater Alpine region and in the Italian peninsula (uncertainty $<$ $0.15-0.2\ km/s$) than in the Ligurian Sea (uncertainty $\sim 0.25-0.4\ km/s$). This difference is certainly due to a less dense path coverage but also to relatively poorer data quality and the complexity of the medium.

A comparison of Fig. 3b and Fig. 3c shows that although uncertainty is generally low where ray coverage is good, a few areas have high uncertainty in spite of good coverage. This happens in areas of strong velocity contrast, for example along the boundaries of the low-velocity anomaly of the Po basin (PB in Fig. 3a). Galetti et al. (2015) attributed such loop-like structures in the error maps to the non-linearity of the forward model. Here instead, we interpret these features as due to the presence of sharp lateral discontinuities in the group-velocity maps. These typical structures in error maps are useful to identify velocity anomalies with uncertain location but well-constrained amplitude.

3.4 Benefits of the transdimensional inversion

The inversion scheme that we used to derive the 2-D group-velocity maps is similar to the one used by Bodin et al. (2012). This procedure has been successfully adapted to our study region despite its large size and the high volume dataset. The dynamic parameterization with Voronoi cells with variable geometries allowed the inversion process to accommodate the irregular distribution of data.

As shown in Supplementary Fig. S3, the 2-D transdimensional inversion outperforms commonly used linearized and regularized inversions. First, this approach allows the computation of group-velocity maps together with their posterior uncertainties that are required to constrain the 3-D V_s model. Second, linearized inversions require explicit parameterization and regularization that often rely on subjective choices. Such a regularization stabilizes the solution in poorly resolved areas, but tends to smooth lateral discontinuities and to bias the resulting solution. These problems do not arise within a Bayesian framework since the degree of smoothing and damping of the solution is naturally driven by the data noise level as well as the heterogeneity of the medium.

The number of Voronoi cells self-adapts to the level of structure present in the data. We show in Supplementary Fig. S4 the posterior distribution on the number of Voronoi cells. We also show the evolution of the model misfit function along the Markov chain and the posterior distribution of the traveltime misfit (Supplementary Fig. S5). We further assess the resolution power of the method by showing results from a synthetic checkerboard test (Supplementary Fig. S6).

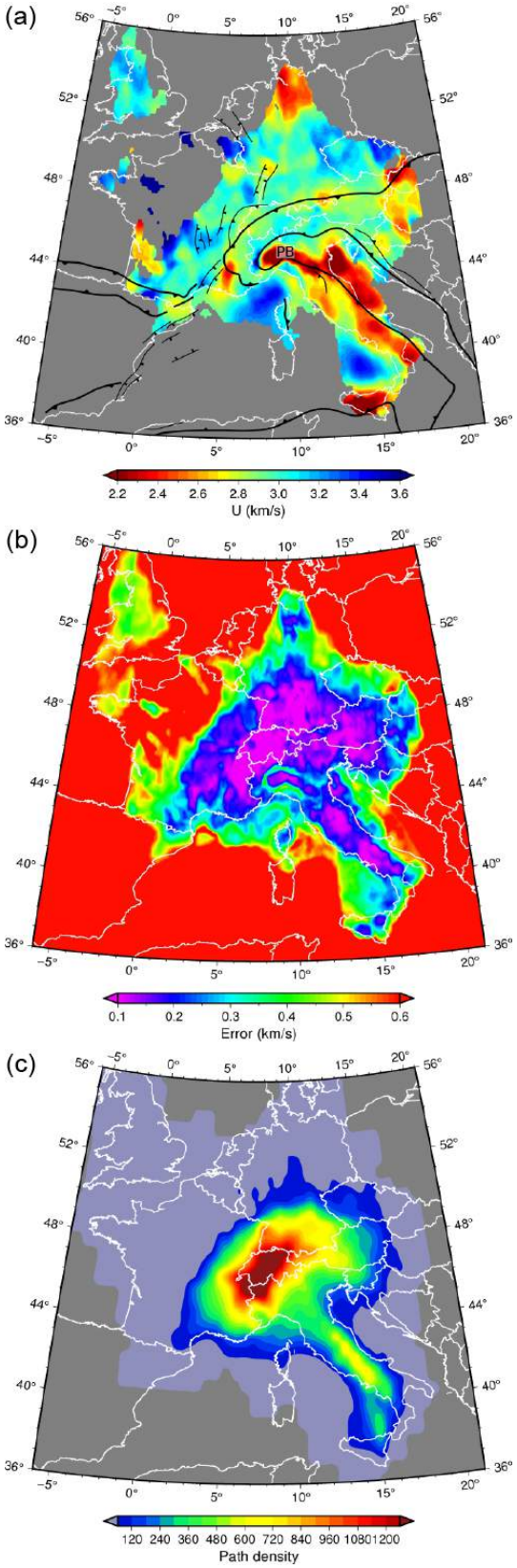

Figure 3. (a) Group-velocity map (average solution) obtained from the *rj-McMC* tomography at $15\ s$ period, showing regions with error $< 0.5\ km/s$. (b) Estimated error map (standard deviation of the ensemble of sampled velocities). (c) Corresponding path density map (number of paths crossing each $0.15° \times 0.15°$ cell).

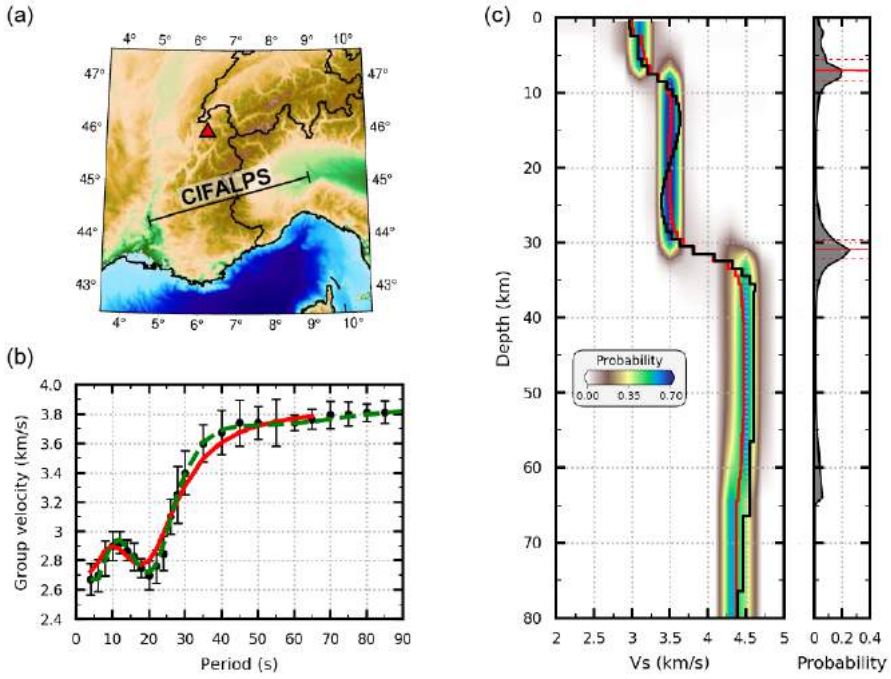

Figure 4. Example of the inversion process for V_s. (a) Location map of the selected grid point (red triangle); For reference, the black line shows the Cifalps profile discussed in section 5. (b) group-velocity dispersion curve of Rayleigh waves (fundamental mode) for the selected grid point; Black: observed dispersion curve with its uncertainties; Red: predicted dispersion curve for the average Bayesian model; Green: predicted dispersion curve after the subsequent linear inversion. (c) Resulting velocity models; Left: posterior probability distribution on shear-wave velocity from the Bayesian inversion (background colors), weighted average solution model (posterior mean) predicted from the probabilistic scheme (red line) and final solution model predicted from the linear inversion (black line). Right: posterior probability distribution on layer boundaries resulting from the Bayesian inversion. The two peaks outlined by red horizontal bars at $7-8\ km$ and $31-32\ km$ depths correspond to the sediment basement and to Moho; The dashed red bars indicate the uncertainty on the boundary depth estimate approximated by the 1σ width.

4 INVERSION FOR SHEAR-WAVE VELOCITY

We used 2-D group-velocity maps and their uncertainties to build a 3-D V_s model of the crust and upper mantle of the Greater Alpine region in two steps. We first computed a 3-D probabilistic V_s solution that gives at each location the probability distribution of V_s and the probability of having an interface as a function of depth. Second, we computed the final V_s model (with a single V_s value at each depth) by refining the probabilistic model using a linear inversion at each pixel, as initially introduced by Macquet et al. (2014). This is particularly useful in areas with complex structures such as the Ivrea Body region, where the mean probabilistic model (obtained with an overly simple parameterization) does not fully explain the local dispersion curve.

Layer	$Thickness(km)$	$V_s(km/s)$
Sediments	$0-16$	$1.6-2.9$
Upper crust	$0-24$	$2.6-3.8$
Lower crust	$2-42$	$3.3-4.3$
Mantle	inf	$3.7-4.7$

Table 1. Ranges of layer thickness and shear-wave velocity used to build the set of four-layer models for the grid search. P-wave velocity and density are derived from V_s using Brocher's empirical relationship (Brocher, 2005).

4.1 Construction of the 3-D probabilistic V_s model

To build the 3-D probabilistic model V_s, we first extracted at each location the local Rayleigh-wave group-velocity dispersion curve from the group-velocity maps presented in the previous section. As discussed further, each of these local dispersion curves is inverted from 4 to 65 s for a local 1-D probabilistic V_s depth profile that provides at each depth the probability distribution of the shear-wave velocity and the probability of presence of an interface. This is done using an exhaustive grid search over a set ~ 130 million of four-layer synthetic models. Each individual model is described with a simple parameterization that includes a sedimentary layer, an upper crust, a lower crust and a half-space representing the uppermost mantle. We assume *PREM* Earth model velocities from the Moho depth to 400 km (Dziewonski & Anderson, 1981). Each layer is parameterized by its thickness and S-wave velocity. P-wave velocities and densities are converted from V_s using Brocher's empirical formula (Brocher, 2005). As shown in Table 1, we choose to explore a wide range of four-layer models that allows for slow velocity layers. As discussed in section 4.2, a Bayesian solution (posterior mean) is then extracted by averaging the ensemble of models weighted by their posterior probability. The 1-D inversion problem is also cast in a Bayesian framework, and we evaluate the probability that each synthetic model $\mathbf{m}$ explains the measured local dispersion curve $\mathbf{d}$ using the Gaussian likelihood function

$$p(\mathbf{d}|\mathbf{m}) = \frac{1}{\sqrt{(2\pi)^N |\mathbf{C}|}} \times \exp\left(\frac{-\phi(\mathbf{m})}{2}\right) \tag{6}$$

where N is the total number of measured periods, $\mathbf{C}$ the covariance matrix of data errors and $\phi(\mathbf{m})$ the misfit function. We assume that uncertainties at different periods of the local dispersion curve are uncorrelated. In that case $\mathbf{C}$ has a diagonal form

$$\mathbf{C} = \begin{bmatrix} {\sigma_1}^2 & 0 & 0 \\ 0 & \dots & 0 \\ 0 & 0 & {\sigma_N}^2 \end{bmatrix} \tag{7}$$

where σ_i is the posterior uncertainty on the group velocity at period i, estimated from the transdimensional group-velocity inversion (see section 3.3).

The misfit $\phi(\mathbf{m})$ between the candidate synthetic dispersion curve $g(\mathbf{m})$ and the local observed dispersion curve is estimated according to the Euclidean distance

$$\phi(\mathbf{m}) = (g(\mathbf{m}) - \mathbf{d})^T \mathbf{C}^{-1} (g(\mathbf{m}) - \mathbf{d}) \tag{8}$$

By substituting (7) and (8) into (6), we obtain the discrete form

$$p(\mathbf{d}|\mathbf{m}) = \frac{1}{\prod_{i=1}^{N} \sqrt{2\pi}\sigma_i} \times \exp\left(\sum_{i=1}^{N} \frac{-(g_i(\mathbf{m}) - d_i)^2}{2{\sigma_i}^2} \right) \tag{9}$$

This likelihood function gives the probability of observing the data given a 1-D profile. Here we assume all tested models are equally probable *a priori* (uniform prior distribution), which makes $p(\mathbf{m})$ a constant and allows us to write

$$p(\mathbf{m}|\mathbf{d}) \propto p(\mathbf{d}|\mathbf{m}) \tag{10}$$

At each depth, we therefore estimate the posterior probability of shear-wave velocities by simply weighting each of the tested models by its likelihood value $p(\mathbf{d}|\mathbf{m})$. Since we perform a uniform grid search in a multidimensional space, a large majority of models are not fitting the data, and have a very low posterior value. For practical reasons, we only used the 100×10^3 best fitting models in the ensemble, and assigned a 0 posterior value to the rest. We verified that this way of approximating the Bayesian solution does not modify the mean and variance of the posterior solution.

This allows us to get for each depth the probability distribution of V_s. In the same way, the probability of presence of an interface can be derived from the ensemble of sampled models and their associated likelihood value.

4.2 Construction of the 3-D final V_s model

The ambient-noise Bayesian scheme described above was applied up to 65 s period to better constrain the crustal part of the model while remaining consistent with the four-layer assumption. To improve the fit to the observed dispersion curve and better constrain the upper mantle part of the model, at each location we averaged the ensemble of selected models weighted by their likelihood values to build a deterministic 3-D V_s model that gives a single value of V_s at each location and depth. This is preferable to only getting the most probable V_s value, since this may introduce sharp discontinuities related to the four-layer assumption. This deterministic V_s model was then used as initial model to perform a linearized inversion (Herrmann, 2013). Three iterations were computed in the $4\ s - 150\ s$ frequency band, taking into account the errors on the observed dispersion curves.

This approach has been modified for the marine parts of the model. We used the same probabilistic inversion as for the on-land pixels and we added a surface layer representing the water column to the initial model of the linear inversion. The thickness of the water layer equals the water depth at the given pixel. We kept the parameters of the water layer fixed during the inversion (ρ, V_s and V_p).

4.3 Strengths of the inversion method for V_s

The inversion scheme that we used to derive the 3-D probabilistic V_s model is similar to that used by Lu et al. (2018), but with two significant improvements. First, rather than using a set of 8 million 1-D V_s models at each location, we explored a broader set of 130 million models that allow for velocity inversions at depth. Second, we did not consider the uncertainties of the local dispersion curves σ to be the same at all periods, nor did we consider them as a parameter of the inversion. Instead, σ was evaluated during the 2-D transdimensional group-velocity inversion. Hence, we formulated the likelihood function so that the uncertainties on group velocities σ were taken into account when computing the misfit $\phi(\mathbf{m})$ between the local dispersion curve and the dispersion curves associated to each of the 130 million of synthetic V_s models. Indeed, an underestimation of the noise level contained in the data would limit the range of 1-D V_s model considered as probable since the algorithm would try to fit the observed local dispersion curve too closely. On the other hand, overestimating the noise level would lead to considering irrelevant 1-D V_s models as probable, hence widening the probability distribution of V_s.

Figure 4 presents an example of a 1-D inversion at a pixel located in the Western Alps (Fig. 4a). In Fig. 4b, the local dispersion curve (black points) and its uncertainties are compared with the dispersion curves associated with the Bayesian average model obtained from the probabilistic inversion (red line) and the final V_s model obtained with an additional linear inversion (green line). The probability distribution of V_s and the probability of presence of an interface are shown on the left and right panels of Fig. 4c respectively. The Bayesian solution (weighted average of the best fitting models, see section 4.2) and the final model obtained after a linear inversion are shown with red and black lines respectively.

We observe a rather sharp V_s probability distribution over the whole depth range that we investigated (width $\leq 0.2\ km/s$ for probability $> 50\ \%$). The probability that an interface is present has two main peaks that correspond to the boundary between the sediment layer and the upper crust at $7-8$ km and to the Moho at $31-32$ km. This results in a multimodal distribution on V_s, with a very high standard deviation (same effect as the "loops" in 2-D, see section 3.3).

The dispersion curve associated with the probabilistic average model (red curve) fits well the observed dispersion curve (black points in Fig. 4b) at periods less than 30 s and greater than 50 s.

However, between 30 s and 50 s where the Rayleigh waves are mostly sensitive to the Moho depth, the posterior mean solution does not completely explain the data, even if it is still compatible with the observed dispersion curve when taking into account the uncertainties. This highlights that in the most complex areas, using a grid search over a library of 130 million four-layer models is insufficient to completely describe the complexity of the medium.

However, in this case, the reference probabilistic model is a relevant initial model for the linear inversion: as shown on Figure 4b, the dispersion curve associated with the final model obtained after a linear inversion fits well with the observed dispersion curve in the whole $4 - 90$ s period range.

4.4 Results: 3-D V_s model

We have derived a quasi-3-D shear-wave velocity model by assembling all 1-D individual models. This new large-scale model has a particularly good resolution over the Greater Alpine region where the density of stations is highest. We have evaluated the reliability of the V_s model by computing the data misfit reduction for each pixel.

Figure 5 presents depth slices at 6, 15, 30 and 60 km in the final 3-D V_s model. The 6-km depth slice in Fig. 5a is consistent with the geological map. We retrieve the main anomalies that we previously discussed on the 8 s map of Fig. 2a, in particular the thick sedimentary basins with velocities lower than 2.7 km/s (Po and North-Adriatic basins, Liguro-Provençal basin, Southeast-France basin and Vienna basin).

At 15-km depth (Fig. 5b), the Ivrea Body is visible as a high-velocity anomaly with V_s in the range $4 - 4.1$ km/s. The Liguro-Provençal basin is associated with high velocities greater than 4 km/s, indicating a shallow Moho. Another striking feature is that at this depth the Adriatic crust exhibits lower velocities ($3.1 - 3.2$ km/s) than European upper crust ($3.3 - 3.5$ km/s).

The 30-km depth slice (Fig. 5c) underlines the variations in crustal thickness, with low velocities (3.5 km/s) in the mountain belts such as the Alps and Apennines. The 60-km depth slice shows a strong low-velocity anomaly ($V_s < 4$ km/s) at the location of the Ivrea Body (IB), in sharp contrast to the shallower high-velocity anomaly. The Apennines, the Northern Adriatic and Sicily have higher velocities ($V_s > 4.6$ km/s) than the Alpine belt and its surrounding regions to the north and west. The Liguro-Provençal basin and the Tyrrhenian Sea have rather low velocities of $4.1 - 4.3$ km/s. The low velocities ($4 - 4.2$ km/s) beneath the volcanic regions and the grabens of the French Massif Central (McF) are probably related to high temperature anomalies in the uppermost mantle.

Supplementary Fig. S7 shows three depth sections in our shear-wave velocity model, along the Cifalps and ECORS-CROP reference profiles in the Western Alps, and the alpine segment of the

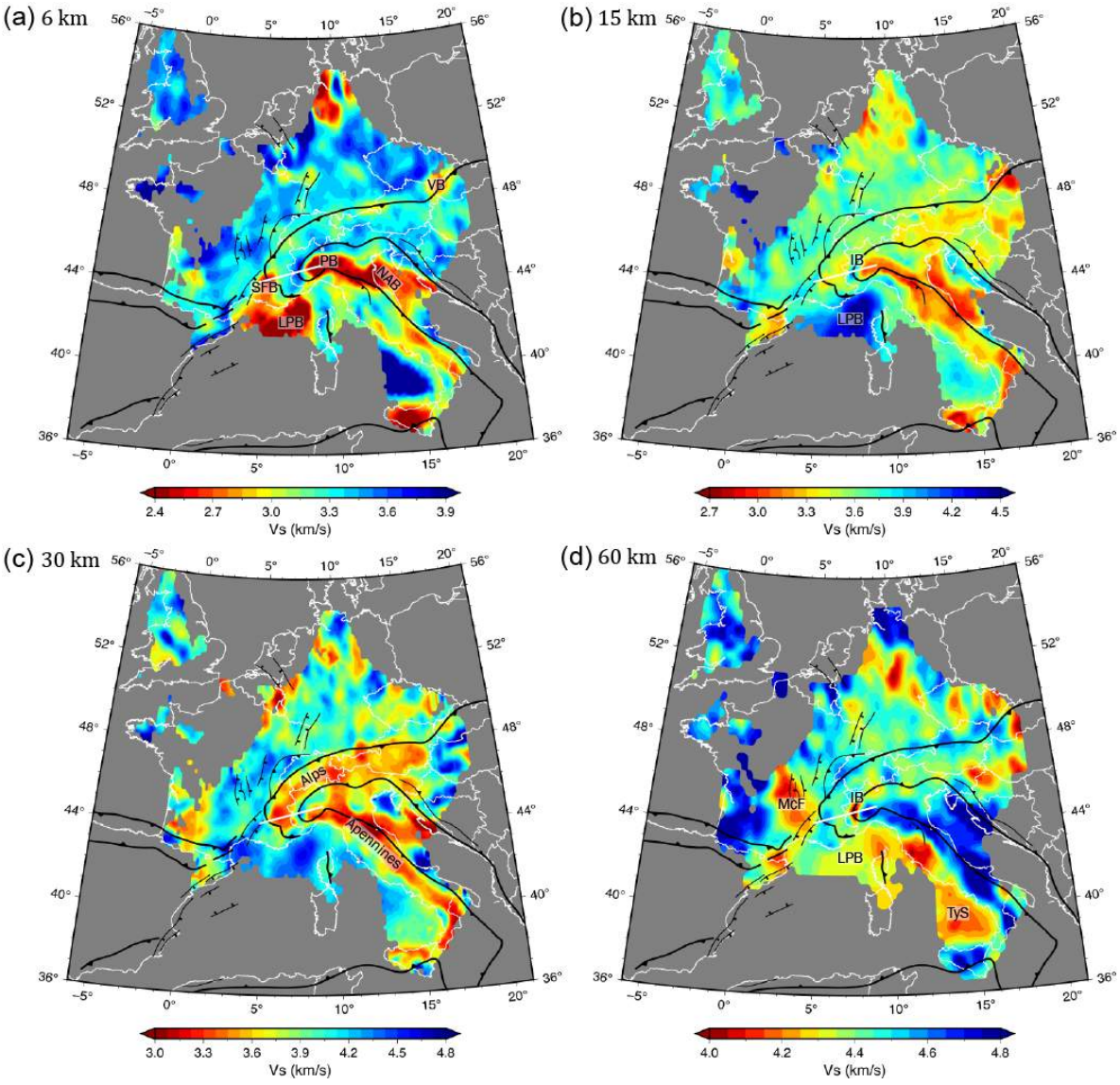

Figure 5. Depth slices in the final V_s model at 6, 15, 30 and 60 km. Only regions with 1σ error $< 8\,\%$ are shown. Black lines show the main geological boundaries as defined in Fig. 1a. The white line shows the Cifalps profile discussed in section 5. IB: Ivrea geophysical body, LPB: Liguro-Provençal basin, McF: Massif Central, NAB: North-Adriatic basin, PB: Po basin, SFB: Southeast-France basin, TyS: Tyrrhenian Sea, VB: Vienna basin.

EASI profile in the Eastern Alps (Hetényi et al., 2018b). These sections document strong along-strike variations in the internal structure of the crust and the Moho geometry.

5 DISCUSSION: FOCUS ON THE CIFALPS TRANSECT

This discussion is focused on the Cifalps cross-section in the South-Western Alps (location in Fig. 4a), which has been the target of a number of joint geophysical-geological studies in the last few years.

The Cifalps transect is therefore a perfect case study to assess the reliability of our new crustal-scale model and to document its potential in terms of geological interpretation.

The Cifalps temporary seismic experiment ($2012-2013$) aimed at imaging the lithospheric structure of a part of the Alpine arc that had not been previously investigated by major geophysical studies (Zhao et al., 2015). It involved a dense quasi-linear profile of 46 broadband stations ($5-10$ km spacing) and 10 off-line stations (Zhao et al., 2016). The dataset has been used in a number of seismic tomography and seismotectonic studies, which results have been interpreted in combination with gravity, tectonic, petrological and petrophysical data (see review in Malusà et al., 2021). The resulting lithospheric-scale geological-geophysical cross-section has therefore become one of the best-documented sections across the Alps. Based on P receiver functions (*RF*), Zhao et al. (2015) provided the first seismological evidence of continental subduction in the Alps, with the detection of P-to-S converted waves at the European Moho at $75-80$ km depth beneath the westernmost Po plain. Zhao et al. (2015) proposed an interpretative geological cross-section that was later refined based on the P-wave velocity model of Solarino et al. (2018) and on the S-wave velocity model of Zhao et al. (2020). The latter imaged a deep low-velocity anomaly at $50-70$ km depth in agreement with the deep P-to-S conversion in *RF* data.

5.1 Model robustness

5.1.1 Data fit and uncertainty assessment

Figures 6a-b show sections of group velocity (as a function of period) and shear-wave velocity (as a function of depth) along the Cifalps profile. In the western part of the cross-section ($40-140$ km distance range), the European continental crust is marked by low group velocities at $5-25$ s period that result in low S-wave velocities over the entire crust, including a low-velocity zone (*LVZ*) in the lower part of the crust (white star in Fig. 6b). By contrast, the $180-270$ km distance range is featured by anomalously high values both in group velocity ($U > 3$ km/s in a broad period range) and in S-wave velocity (4.0 km/s at 10 km depth). These anomalies correspond to the Ivrea high-velocity high-density body (IB) that was discovered in the early 1960's (Closs and Labrouste, 1963). Our V_s model of the Ivrea body region is similar to the one computed by Zhao et al. (2020) using a different transdimensional inversion scheme. It also exhibits a deep *LVZ* with $V_s \leq 3.9$ km/s at $50-80$ km depth, as an extension of the lower part of the European continental crust (black star in Fig. 6b). The step geometry of the velocity contours on the eastern flank of the Ivrea body that may correspond to back-thrusts of the collision belt is however a new feature that did not appear in the model of Zhao et al. (2020). This may indicate that our model is better resolved. Figure 6c shows the probability densities for an interface to be present. The basements of the Southeast basin of France in the WSW

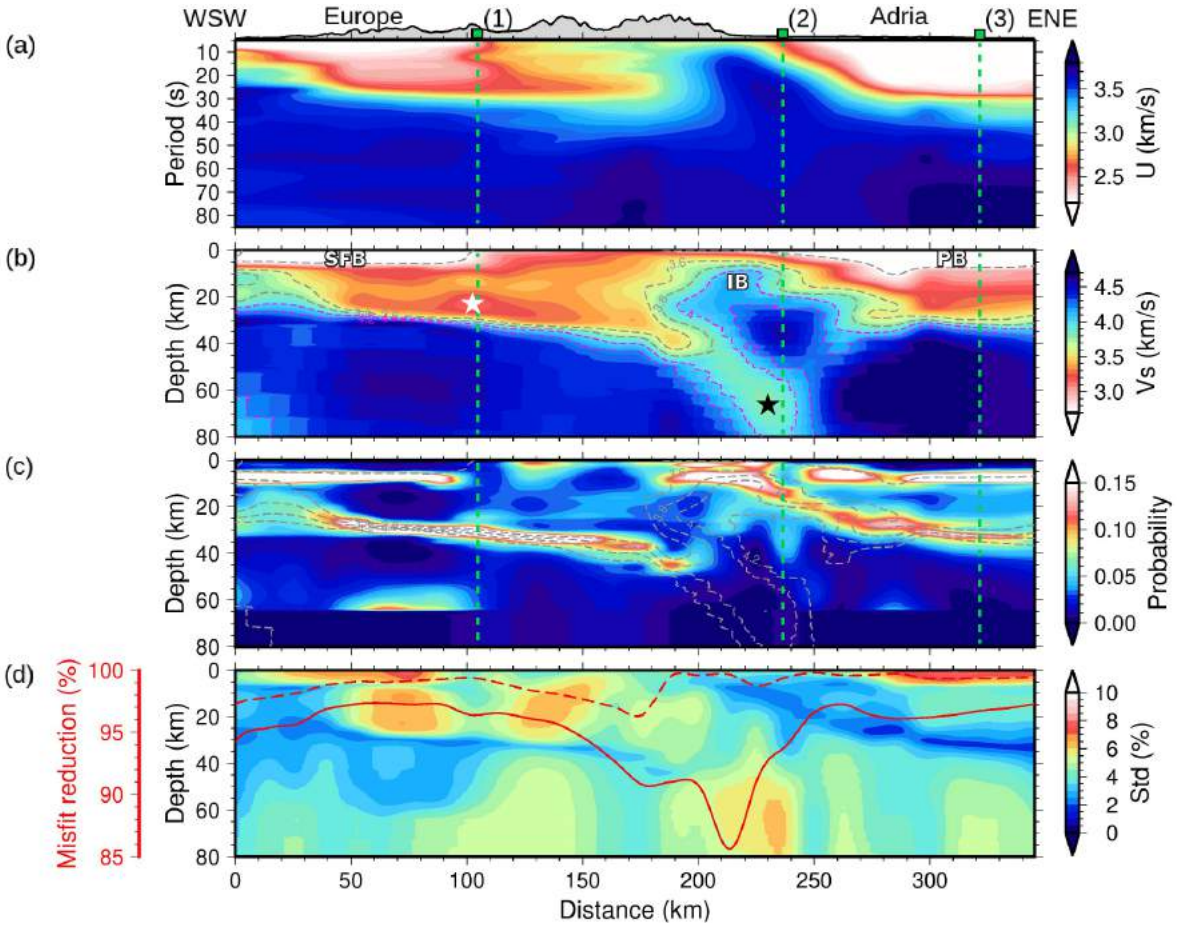

Figure 6. Depth sections of observations and inversion results along the Cifalps WSW-ENE profile (location in Fig. 4a). (a) Rayleigh-wave group velocities obtained from the Hierarchical Bayes reversible-jump tomography at grid points located along the profile. Green vertical dashed lines indicate locations of pixels (1), (2) and (3) discussed in the text. (b) Final shear-wave velocity section. The 2.7, 3.6 and 3.8 km/s velocity contours are shown as gray dashed lines while the pink dashed lines indicate the 4.0 and 4.2 km/s velocity contours. The white and black stars mark low-velocity anomalies discussed in the text. (c) Posterior probability density of presence of a layer boundary obtained from the Bayesian inversion. The dashed lines show the same velocity contours as in (b). (d) Color map: model uncertainties approximated for each location and at each depth by the 1σ value of the ensemble of most probable models normalized by the V_s value at this grid point/depth. The thick red line indicates the total misfit reduction after the Bayesian inversion while the red dashed line indicates the total misfit reduction after the linearized inversion. IB: Ivrea geophysical Body, PB: Po basin, SFB: Southeast-France basin.

and of the Po basin in the ESE are marked by strong velocity gradients, hence strong probability that an interface is present. This is also the case for most of the European Moho at $25 - 40$ km depth, and for the very shallow Moho on top of the Ivrea mantle body that extends towards the ENE to the normal Adriatic Moho at a depth of ~ 35 km beneath the Po basin.

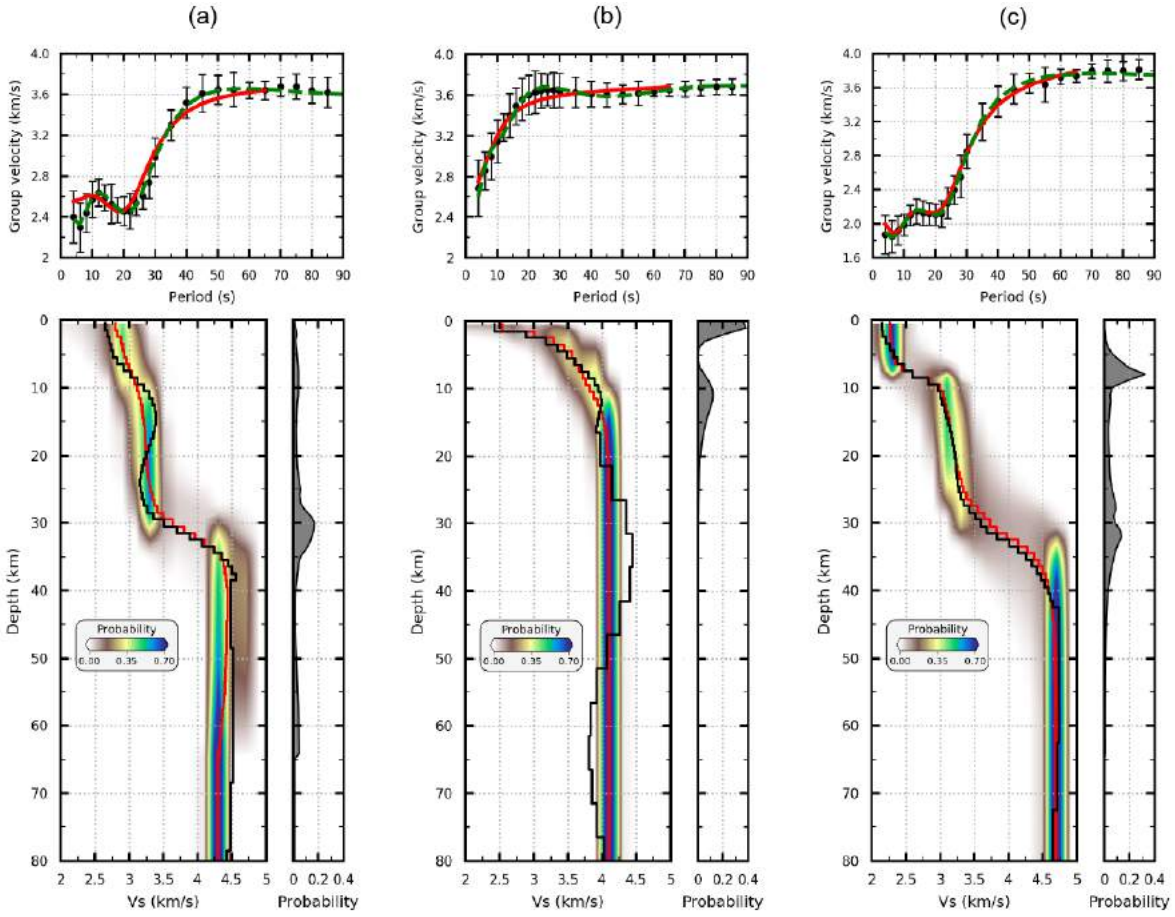

Figure 7. Results of the inversion for V_s at pixels 1 (panels a), 2 (panels b) and 3 (panels c). Pixel locations are indicated in Fig. 6a). The top panels show observed (black) and predicted dispersion curves (red: from the Bayesian inversion; green: from the linear inversion). The bottom panels show: (left) probability density of V_s (color map) and predicted V_s models (red: probabilistic average model; black: final model); (right) probability density of interface presence.

As shown in Fig. 6d, the misfit reduction between the observed dispersion curves and the dispersion curves computed from the final V_s model (dashed red line) is everywhere higher than the misfit reduction computed for the Bayesian model, used as initial model for the linearized inversion (solid red line). The misfit reduction is strongest in the Ivrea body region (distance $170-240\ km$), where the uncertainty on the Bayesian V_s model is strongest at large depth ($50-80\ km$). Fig. 6d also shows that sedimentary basins exhibit the largest uncertainties of $\sim$ 7-8 %, while the smallest uncertainties are observed along the Adriatic Moho. A similar small uncertainty is observed along the European Moho up to $180\ km$ distance where the Moho dip increases abruptly. These lateral changes in model uncertainty and misfit differences between the Bayesian and the final V_s model indicate that in the most complex areas none of the 130 million four-layer models that have been explored during the prob-

abilistic inversion can explain completely the observed dispersion curve. In this case the linearized inversion is required to refine the V_s model.

To further investigate the robustness of our final model and its lateral variations, we analyze in Fig. 7 the outputs of 1-D inversions for V_s at three representative locations labelled (1), (2) and (3) in Figures 6a-b. Figure 7 shows first of all that dispersion curves computed from the final models (green curves) match observations well. The gain with respect to the results of the Bayesian inversion (red curves) is higher at pixels (1) and (2) (Fig. 7a-b), which have a complex crustal structure that deviates more from the three-layer crust assumption than pixel (3) (Fig. 7c).

At pixel (1), the linearized inversion results in a low-velocity zone at $15-30\ km$ depth that better explains low group velocities at $15-25\ s$ period. Pixel (2) is located in the westernmost Po plain on the eastern flank of the Ivrea high-velocity body. Compared to the average probabilistic model (red curve), the linearized inversion leads to slightly higher velocities of $4.0\ km/s$ at $\sim 10\ km$, even higher velocities at $25-45\ km$ depth ($4.4\ km/s$) and lower velocities ($3.8\ km/s$) at $52-77\ km$ depth. The final modeled dispersion curve (green curve in Fig. 7b top) fits the observations better than the dispersion curve computed from the average probabilistic model (red curve). The example pixels (1) and (2) further confirm that the Bayesian inversion and its four-layer model assumption fail to explain such complex group-velocity data, while the final step of linearized inversion does a better job thanks to its fair initial model.

Such strong differences between the average probabilistic model and the final model are not observed at pixel (3) because its V_s model has a "normal" layered structure with a positive velocity gradient (Fig. 7c). The very low velocities ($\leq 2.2\ km/s$) from 0 to $7-8\ km$ depth are the signature of the thick Po basin.

5.1.2 Benefits of our hybrid inversion scheme

Unlike Lu et al. (2018) and most ambient-noise tomographies, we used a 2-D transdimensional inversion for group-velocity maps to avoid biases arising from explicit regularisation. The Bayesian nature of this inversion also allows for a robust quantification of the uncertainties on group velocities and hence local dispersion curves. Unlike Zhao et al. (2020) who used a full transdimensional approach in the inversion for V_s, we performed an exhaustive grid search over all possible 4-layer models, followed by a linear inversion. This hybrid methodology limits the complexity of resulting V_s model while giving enough freedom to the inversion to actually fit the data. It also provides uncertainties on V_s and the probability of having an interface at given depths. To document the benefits of our approach, supplementary Fig. S8 and its comments compare our model to the one by Zhao et al. (2020) on depth sections along the Cifalps and ECORS-CROP reference profiles. The two models exhibit

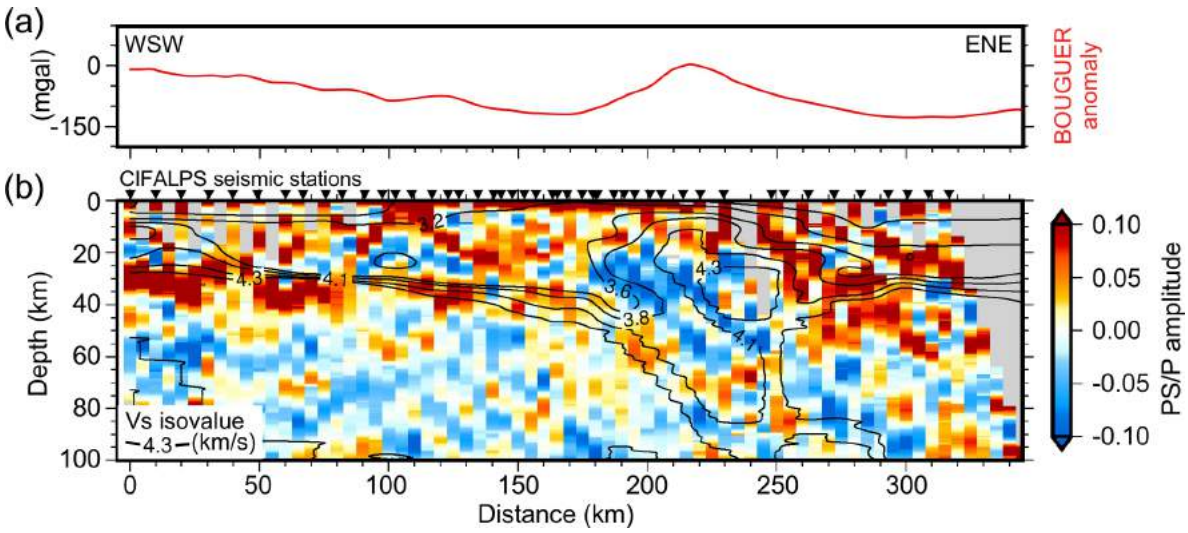

Figure 8. Comparison of our V_s model along the Cifalps line with independent geophysical data. (a) Bouguer gravity anomaly extracted from the AAGRG model (AlpArray Gravity Research Group; Zahorec et al., 2021). (b) Receiver-function CCP depth section migrated using our V_s model; The black plain lines are the 2.7, 3.2, 3.6, 3.8, 4.1 and 4.3 km/s contours of our V_s model; Locations of stations projected onto the profile are shown as black inverted triangles (station map shown in Fig. 9a).

differences that can be attributed to the improved data coverage in the western part of the study region, or to the inversion scheme. The results of our inversion is more in line with previous geophysical data. Moreover, the hybrid character of our inversion makes it much less computationally expensive than pure transdimensional inversion. Therefore, we could compute a robust 3-D V_s model at the scale of Western Europe from such a large volume of data using reasonable computational resources.

5.2 Comparison with other geophysical data

In Figure 8, we compare the depth section through our V_s model along the Cifalps profile with the Bouguer anomaly (Fig. 8a) and the receiver-function CCP migrated depth section (common conversion point; Zhu, 2000) computed from the Cifalps dataset (Zhao et al., 2015) and migrated using our V_s model (Fig. 8b).

A receiver-function section displays teleseismic P-to-S converted waves (P_s) at velocity discontinuities beneath the stations, with positive amplitudes indicative of velocity increase with depth, and negative polarities indicative of velocity decrease with depth (Vinnik, 1977). Unlike Zhao et al. (2015) who used a four-segment 1-D migration model, we used the 2-D V_s model derived from our ambient-noise tomography (shown as velocity contours in Fig. 8b) to perform the time-to-depth CCP migration of receiver functions.

The maximum of the Ivrea gravity anomaly (positive Bouguer anomaly in Fig. 8a) coincides well

with the top of the high-V_s anomaly (3.8 and 4.1 km/s contours in Fig. 8b). The consistency between the V_s model and the CCP section is outstanding, considering that the sensitivity of surface waves to sharp velocity boundaries is rather weak. The $4.2 - 4.3$ km/s velocity contours are fairly consistent with the European Moho, which is characterized by a clear P_s phase of positive polarity at distances $0 - 200$ km. The agreement is not that good at $200 - 250$ km distance where the $4.2 - 4.3$ km/s contours are deeper than the deepest P_s phases at $70 - 80$ km depth that were interpreted by Zhao et al. (2015) as evidence of continental subduction of Europe beneath Adria. The *RF* data quality is poorer under the Po basin, making comparison with V_s contours difficult. In addition, the 3.6 and 3.8 km/s contours match the negative polarity P_s phases observed above the European Moho at distances $180 - 250$ km, which were interpreted by Zhao et al. (2015) as traces of an "inverted" Moho between the Ivrea mantle body on top and the European crust below. We conclude from the match of the $4.2 - 4.3$ km/s velocity contours with the European Moho that these contours are an accurate proxy of the autochthonous Moho, while the 3.8 or 4.0 km/s contours are more adequate to characterize the Moho at the top of the serpentinized Ivrea body.

We have seen in Fig. 6c that the probability of presence of an interface is a reliable marker of a strong velocity contrast. For instance, the probability is lower for the Adriatic Moho than for the European Moho, due to a lower velocity gradient on the Adriatic side (Fig. 7a and Fig. 7c). This correlation with the velocity gradient is however not valid everywhere, as for instance at the top of the Ivrea body anomaly where the probability is high while the gradient is rather smooth (Fig. 7b). Hence, the probability of presence of an interface is an accurate proxy not only for the base of sedimentary basins, but also for delineating the crust-mantle boundary of Adria and Europe, and highlighting interfaces with weak velocity gradient such as the top of the Ivrea body. However, Fig. 6c shows that the probability section is almost blind inside the subduction complex due to its very complex structure, which means that interface probability cannot be considered as a universal proxy for Moho. By contrast, the comparison between the V_s section and the *RF* section has confirmed that the 4.2 or 4.3 km/s iso-velocity contour is better suited to delineate deep discontinuities associated with the subduction of the European lithosphere. In future studies, we will therefore rather exploit the 4.3 km/s contour as a proxy of Moho to delineate its 3-D depth variations.

5.3 Crustal-scale geological interpretations

In Figure 9, we propose a geological interpretation of the shear-wave velocity section along the Cifalps profile that also builds on surface geological observation, on previous joint geophysical-geological works summarized in Malusà et al. (2021), on the *RF* section of Fig. 8b and on hypocenter locations by Eva et al. (2015) and Malusà et al (2017).

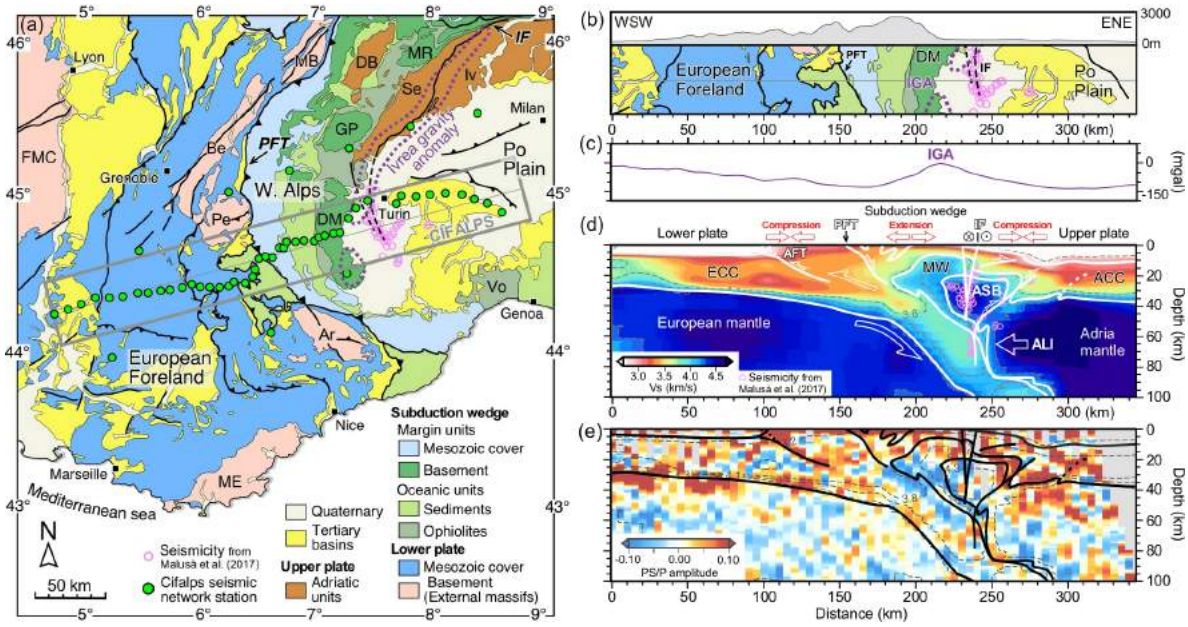

Figure 9. Geological and tectonic settings of the study area along the Cifalps transect. (a) Geological map of the W-Alps with location of the Cifalps seismic network (white rectangle in Fig. 1b). Earthquake epicenters with depth $> 20\ km$ beneath the westernmost Po plain are shown as pink open circles (after Eva et al., 2015 and Malusà et al., 2017). The Ivrea gravity anomaly is represented by the $0\ mGal$ contour (dashed purple line) from Bigi et al. (1990). The continental crust units of the European plate (lower plate) are indicated by: Ar, Argentera; Be, Belledonne; MB, Mont-Blanc; Pe, Pelvoux; ME, Maures-Estérel; FMC, French Massif Central. The Adriatic units (upper plate) are indicated by: DB, Dent Blanche; Iv, Ivrea-Verbano; Se, Sesia. The internal crystalline massifs of the subduction wedge are indicated by: DM, Dora Maira; GP, Gran Paradiso; MR: Monte Rosa; Two major tectonic limits are also indicated: IF, Insubric Fault; PFT: Penninic Frontal Thrust. (b) Topographic profile and geological map (extracted from (a)) along the Cifalps transect. (c) Bouguer gravity anomaly extracted along the profile (same as Fig. 8a). IGA: Ivrea Gravity Anomaly. (d) Crustal-scale interpretation of the V_s depth section along the Cifalps transect. The main geological interfaces corresponding to lithological units and tectonic structures are underlined in white (see interpretation in text). This interpretation shows the subduction of the European lithosphere toward the East below the Adria lithospheric mantle. The European continental crust (ECC) is continuous down to $100\ km$ depth. We observe separation of the Adria lithospheric mantle into two main bodies: (1) The deeper part ALI (Adria lithospheric indentor) acts as a horizontal indentor that deformed the European slab and enabled the activation of the Alpine Frontal Thrust (AFT). (2) The upper part ASB (Adria seismic body) acts as a vertical indentor controlling the exhumation of the mantle wedge (MW) and locating the deep seismicity along the Insubric Fault (IF) system. In this interpretation, the Adriatic continental crust (ACC) is deformed by top-to-northeast thrusts. In the global tectonic convergence, the crustal-scale geometry deduced from the V_s model controls the partitioning of the strain field (red arrows). The crustal compartment located between the IF and PFT tectonic structures records extension while the two other compartments record compression. (e) Crustal-scale interpretation plotted as black lines on the receiver-function CCP depth section of Fig. 8b.

In the following subsections, we emphasize a number of first-order features related to the geometry of structures at crustal scale, to the deformation and thermicity of the lithosphere, and to the link between the lithospheric structure and the strain field.

5.3.1 Geometry of structures at lithospheric scale

The geology of the Western Alps (Fig. 9a) results from the convergence of two lithospheric plates (Polino et al., 1990; Dumont et al., 2012). To the west, the European margin corresponds to the lower plate, which subducted beneath the Adriatic upper plate to the east. Between these two continental domains, the subduction wedge developed by the juxtaposition of oceanic sediments and crustal fragments (Lardeaux et al., 2006; Schwartz et al., 2009; Agard et al., 2021) with units originating from the two continental margins (Fig. 9a). This prism is bounded by two major crustal-scale faults: to the west the Penninic Frontal Thrust (PFT) and to the east the dextral strike-slip Insubric Fault (IF). The European foreland accommodates the convergence through the propagation of a fold-and-thrust-belt system associated with the development of Cenozoic sedimentary basins (Ford et al., 1999). These basins are further deformed, uplifted and partially eroded during the westward propagation of compressional structures. This compressional deformation is localized at depth along crustal-scale thrusts leading to the exhumation of the External Crystalline Massifs in thick skin tectonic mode (e.g., Jourdon et al., 2014; Schwartz et al., 2017). To the East, the Po plain is affected by top-to-northeast back-thrusts allowing the uplift and erosion of Cenozoic basins (Mosca et al., 2010).

The V_s model documents the subduction of the European lithosphere towards the east below the Adria lithospheric mantle, marked by a continuous European continental crust down to a minimum depth of $100\ km$. This continental crust is featured by a progressive increase of V_s with depth from $3.4 - 3.5\ km/s$ at $20 - 30\ km$ to $4.2\ km/s$ at $100\ km$ interpreted as resulting from the densification of continental rocks during their progressive eclogitization.

Under the westernmost part of the European foreland, high crustal V_s values of $3.6 - 3.8\ km/s$ and a slight Moho uprise (iso-velocity contour $V_s = 4.3\ km/s$) indicate crustal thinning beneath the Rhône valley consistently with the formation of the Western European Cenozoic Rift System (Ziegler, 1992).

One of the most striking features of the section is a standard crustal thickness of $\sim 30\ km$ below the frontal part of the External Massifs, increasing to $\sim 50\ km$ below the PFT. This observation is in line with other recent geophysical models along the Cifalps profile that exhibit very little crustal thickening of the External Alps (e.g., Malusà et al., 2021).

Beneath the Ivrea Gravity Anomaly (IGA in Fig. 9c), located along the Insubric Fault and extending southwards beneath the Internal Crystalline Massif of Dora Maira (Fig. 9a-b), the upper part of

the subduction wedge is likely formed by stacking of crustal slices extracted from both the continental and oceanic crusts. This subduction wedge overlies the mantle wedge (MW, Fig. 9d) at a depth of about $10\ km$. This mantle wedge, documented by shear-wave velocities ranging between ~ 3.8 and $4.0\ km/s$, may be composed of partially serpentinized mantle of Adriatic origin produced by hydration above the subducted oceanic units. Below the subduction wedge, a superposition of several mantle bodies with different geophysical signatures is observed, which suggests the superposition of two petrological Mohos: a first one characterized by a reverse V_s gradient with a negative polarity in the receiver function (*RF*) section (Fig. 9e). This "inverted Moho" corresponds to the subduction interface between the European slab and the mantle wedge. The second, deeper Moho corresponds to the European Moho itself, steeply dipping due to subduction.

5.3.2 Deformation and thermicity

The deformation is dominated by compressive structures occurring in both forelands of the chain, with top-to-the-west thick-skinned propagation on the western side of the belt, rooted in the lower crust. A major thrust is well marked in the *RF* section as a set of positive-polarity signals down to $25\ km$ depth that connects at the surface with the thrust (Fig. 9e). We name it the Alpine Frontal Thrust (AFT). Similar structures occur on the eastern side of the Alps, below the Po plain, which either do not outcrop or may merge with the frontal Po thrust system. The rooting of these peripheral thrusts appears to occur at different depth levels. We propose that the AFT becomes horizontal in the lower crust, where V_s has very low values $< 3.4\ km/s$ (Fig. 9d), which would be consistent with the more ductile rheology of the European lower crust. In contrast, the step-like shape of the V_s contours in the eastern side suggests that the Adriatic Moho and continental crust (ACC, Fig. 9d) are significantly offset by the main top-to-northeast thrusts. This difference in deformation style between the European crust and the Adria crust is in agreement with a different thermal state, revealed by different V_s layouts in the lithospheric mantle domains. The higher and more homogeneous shear-wave velocities observed in the Adria mantle may indicate a colder state leading to a more rigid behavior. In this context, the Adria lithospheric mantle behaves as a deep horizontal indentor (the Adria Lithospheric Indentor or ALI, Fig. 9d) buttressing the European slab along a $25\ km$-high vertical boundary.

As a result of this deep indentation, the mantle wedge is vertically indented by an intermediate, non-serpentinized rigid mantle body with $V_s \sim 4.2 - 4.4\ km/s$ that localizes most of the deep seismicity ($> 20\ km$) below the westernmost Po plain (pink open circles in Fig. 9a, b, d; Eva et al., 2015; Malusà et al., 2017). This rigid body is named Adria Seismic Body (ASB). We relate the vertical seismic swarm in the ASB to the rooting zone of the Insubric Fault.

5.3.3 Link between the geometry of lithospheric structures and the strain field

In the framework of plate tectonics and convergence between Europe and Adria, the observed split of the Adriatic lithospheric mantle into two units (ASB and ALI) would be responsible for the partitioning of the deformation at lithospheric scale. The deeper part of the Adria mantle (ALI) horizontally indents the European slab. This results both in lithospheric loading and in lithospheric shear deformation propagating westwards to reach the upper crust beneath the European foreland, corresponding to the activation of the Alpine Frontal Thrust (AFT). The upper part of the Adria mantle (ASB) was pushed upwards and maintained in a high structural position by the ALI horizontal indentation. In turn, the ASB acted as a vertical indentor responsible for the deformation and exhumation of the subduction wedge units.

This geometry leads to a partitioning of the active deformation on both sides of the Insubric Fault (Fig. 9d). To the east of the IF, the subduction wedge is backthrusted onto the Adria crust and the Adria lithosphere is significantly shortened (Mathey et al., 2020). In contrast, to the west of the IF, extensional deformation dominates in a crustal compartment bounded by the IF and the PFT (Mathey et al., 2020), as a result of vertical indentation. This latter thrust was reactivated since at least $3-4$ Ma, and it is still currently undergoing extensional deformation (Bilau et al., 2021).

6 CONCLUSION

The high density and rather homogeneous coverage of permanent European broadband networks complemented with the AlpArray temporary network and quasi-linear dense arrays such as Cifalps, Cifalps-2, and EASI were key in our derivation of a high-resolution shear-wave velocity model of the Alpine mountain belt and its forelands. We used four years of continuous seismic noise recorded by $\sim$ 1550 broadband seismic stations, which led to 1.1 million cross-correlations of vertical noise records. Rayleigh-wave group-velocity dispersion curves were measured in the $4-150$ s period band and 2-D group-velocity maps and their uncertainties were computed using a data-driven transdimensional inversion that allows the local resolution to self-adapt to the path density and to the variability of information contained in group-velocity measurements. At each location of our $0.15^\circ \times 0.15^\circ$ grid, the local group-velocity dispersion curve and its associated uncertainties were inverted jointly in a Bayesian approach to derive a quasi-3-D probabilistic shear-wave velocity model. This model was further refined using a linear inversion.

The best-resolved part of our 3-D V_s model covers the Alpine range, its forelands and the Ligurian Sea. We showed on the Cifalps traverse of the South-Western Alps that the resolution of our model makes it possible to correlate features of the geophysical model with geological structures mapped at

the surface. This enabled an integrated geological-geophysical interpretation that highlights first-order features related to the subduction of the European lithosphere under the Adriatic lithosphere in the South-Western Alps. One of these key features is the Ivrea geophysical body, which is likely made of a subduction wedge formed by stacking of crustal slices of continental and oceanic origin overlying a mantle wedge likely composed of partially serpentinized Adriatic mantle. Another key feature is the split of the Adriatic mantle lithosphere in two different units. This split could be responsible for the partitioning of the deformation at lithospheric scale.

Following the model verification at the location of the 2-D Cifalps cross-section, our velocity model makes it possible to construct a 3-D, lithospheric-scale geological models of the Alpine belt, extending the geological maps in depth. These models are expected to provide key constraints to conceptual geological-petrophysical models of subduction wedge systems, for example. Such interpretation work has already started for the Western Alps.

Our V_s model can also be used in further geophysical studies, including waveform modelling and full waveform inversion. Our next project is to use this model as an initial model to simultaneously build a 3-D V_p and V_s model of the Alpine lithosphere by joint inversion of surface-wave dispersion data from noise correlations and travel times of body waves emitted by local earthquakes using a 3-D wave-equation tomography. This combination of P-wave and S-wave velocities is required to establish the lithology of rocks buried at large depths.

DATA AVAILABILITY STATEMENT

Our tomographic 3-D model will be available in the Résif products repository (Réseau sismologique et géodésique Français; https://www.resif.fr/en/data-and-products/products-repository/). The inversion code is available on request to the first author.

Waveform data used in this paper belong to the permanent networks with codes AC, BE (Royal Observatory of Belgium, 1985), CA (Institut Cartogràfic i Geològic de Catalunya-Institut d'Estudis Catalans, 1984), CH [Swiss Seismological Service (SED) at ETH Zürich, 1983], CR (University Of Zagreb, International Federation of Digital Seismograph Networks, 2001), CZ (Institute of Geophysics, Academy of Sciences of the Czech Republic, 1973), ES (Instituto Geografico Nacional, Spain, 1999), FR (RESIF, 1995), G [Institut de Physique du Globe de Paris (IPGP) and Ecole et Observatoire des Sciences de la Terre de Strasbourg (EOST), 1982], GB [GEOFON Data Centre, 1993], GR [Federal Institute For Geosciences And Natural Resources (BGR), 1976], IV (INGV Seismological Data Centre, 2006), NL (KNMI, 1993), OE (ZAMG— Zentralanstalt für Meterologie und Geodynamik, 1987), SL (Slovenian Environment Agency, 2001), and UP (SNSN, 1904). We also used data of the temporary AlpArray network (Z3 network, AlpArray Seismic Network, 2015), Cifalps (YP

network, Zhao et al., 2016, and XT network, Zhao et al., 2018) and EASI experiments (XT network, AlpArray seismic network, 2014).

Acknowledgements

This study was partly funded by the SEISCOPE consortium (https://seiscope2.osug.fr), sponsored by AKERBP, CGG, CHEVRON, EQUINOR, EXXON-MOBIL, JGI, SHELL, SINOPEC, SISPROBE and TOTAL, and by the RGF program (Référentiel Géologique de la France, http://rgf.brgm.fr/). It is part of the AlpArray-FR project funded by Agence Nationale de la Recherche (contract ANR-15-CE31-0015) and by Labex OSUG@2020 (Investissements d'Avenir, ANR-10-LABX-56). The Cifalps experiments are funded by the National Natural Science Foundation of China (Grants 41625016, 41888101, and 91955210). Thomas Bodin is funded by the European Union's Horizon 2020 research and innovation program under grant agreement 716542. We warmly thank Yang Lu (USC-SCEC, USA) and Wayne Crawford (IPGP, France) for having shared their tools and for their constructive feedback on our inversion methodology (YL) and on OBS data processing (WC). We are grateful to Helle Pedersen and Rod Bark for their careful reading and corrections of the final version. We thank the Editor, Ana Ferreira, and Sébastien Chevrot and an anonymous reviewer for their insightful comments that helped to improve the manuscript. This study was granted access to the HPC resources of the Dahu platform of the CIMENT infrastructure (https://gricad.univ-grenoble-alpes.fr/), which is supported by the Auvergne-Rhône-Alpes region (grant CPER07-13CIRA), the Labex OSUG@2020 (reference ANR10 LABX56) and the Equip@Meso project (reference ANR-10-EQPX-29-01) of the program 'Investissements d'Avenir' supervised by the Agence Nationale de la Recherche and the HPC resources of CINES/IDRIS/TGCC under allocation 046091 by GENCI. We are grateful to the operators of European permanent seismic networks who make their data available through EIDA (http://www.orfeus-eu.org/data/eida/). The CIFALPS Team includes Coralie AUBERT, Elena EVA, Stéphane GUILLOT, Marco G. MALUSA, Silvia PONDRELLI, Simone SALIMBENI, Stefano SOLARINO, and Liang ZHAO. The Z3 network was operated by the AlpArray Seismic Network Team: György HETÉNYI, Rafael ABREU, Ivo ALLEGRETTI, Maria-Theresia APOLONER, Coralie AUBERT, Simon BESANÇON, Maxime BÈS DE BERC, Götz BOKELMANN, Didier BRUNEL, Marco CAPELLO, Martina ČARMAN, Adriano CAVALIERE, Jérôme CHÈZE, Claudio CHIARABBA, John CLINTON, Glenn COUGOULAT, Wayne C. CRAWFORD, Luigia CRISTIANO, Tibor CZ-IFRA, Ezio D'ALEMA, Stefania DANESI, Romuald DANIEL, Anke DANNOWSKI, Iva DASOVIĆ, Anne DESCHAMPS, Jean-Xavier DESSA, Cécile DOUBRE, Sven EGDORF, ETHZ-SED Electronics Lab, Tomislav FIKET, Kasper FISCHER, Wolfgang FRIEDERICH, Florian FUCHS, Sigward FUNKE, Domenico GIARDINI, Aladino GOVONI, Zoltán GRÁCZER, Gidera GRÖSCHL, Stefan

HEIMERS, Ben HEIT, Davorka HERAK, Marijan HERAK, Johann HUBER, Dejan JARIĆ, Petr JEDLIČKA, Yan JIA, Hélène JUND, Edi KISSLING, Stefan KLINGEN, Bernhard KLOTZ, Petr KOLÍNSKÝ, Heidrun KOPP, Michael KORN, Josef KOTEK, Lothar KÜHNE, Krešo KUK, Dietrich LANGE, Jürgen LOOS, Sara LOVATI, Deny MALENGROS, Lucia MARGHERITI, Christophe MARON, Xavier MARTIN, Marco MASSA, Francesco MAZZARINI, Thomas MEIER, Laurent MÉTRAL, Irene MOLINARI, Milena MORETTI, Anna NARDI, Jurij PAHOR, Anne PAUL, Catherine PÉQUEGNAT, Daniel PETERSEN, Damiano PESARESI, Davide PICCININI, Claudia PIROMALLO, Thomas PLENEFISCH, Jaroslava PLOMEROVÁ, Silvia PONDRELLI, Snježan PREVOLNIK, Roman RACINE, Marc RÉGNIER, Miriam REISS, Joachim RITTER, Georg RÜMPKER, Simone SALIMBENI, Marco SANTULIN, Werner SCHERER, Sven SCHIPPKUS, Detlef SCHULTE-KORTNACK, Vesna ŠIPKA, Stefano SOLARINO, Daniele SPALLAROSSA, Kathrin SPIEKER, Josip STIPČEVIĆ, Angelo STROLLO, Bálint SÜLE, Gyöngyvér SZANYI, Eszter SZŰCS, Christine THOMAS, Martin THORWART, Frederik TILMANN, Stefan UEDING, Massimiliano VALLOCCHIA, Luděk VECSEY, René VOIGT, Joachim WASSERMANN, Zoltán WÉBER, Christian WEIDLE, Viktor WESZTERGOM, Gauthier WEYLAND, Stefan WIEMER, Felix WOLF, David WOLYNIEC, Thomas ZIEKE, Mladen ŽIVČIĆ, Helena ŽLEBČÍKOVÁ.

Supporting information

Additional Figures (S1-S8) and information are presented as the Supplementary Material.

Figure S1. Distance-time plot of noise correlations.

Figure S2. Comparison of the 8-s and 25-s group-velocity maps with sedimentary basins and Moho depth maps.

Figure S3. Comparison with a matrix-based inversion.

Figure S4. Posterior distribution on the number of Voronoi cells.

Figure S5. Inversion misfit.

Figure S6. Checkerboard tests.

Figure S7. Depth sections through the V_s model along reference profiles.

Figure S8. Comparison with the V_s model by Zhao et al. (2020).

References

Agard, P., 2021. Subduction of oceanic lithosphere in the Alps: Selective and archetypal from (slow-spreading) oceans, *Earth-Science Reviews*, **214**, 103517.

AlpArray Seismic Network, 2014. Eastern Alpine Seismic Investigation (EASI) - AlpArray Complimentary Experiment.

AlpArray Seismic Network, 2015. AlpArray Seismic Network (AASN) temporary component.

Bigi, G., Cosentino, D., Parotto, M., Sartori, R., & Scandone, P., 1990. Structural model of Italy and gravity map, *Quad. Ric. Sci.*, **114**.

Bilau, A., Rolland, Y., Schwartz, S., Godeau, N., Guihou, A., Deschamps, P., Brigaud, B., Noret, A., Dumont, T., & Gautheron, C., 2021. Extensional reactivation of the Penninic frontal thrust 3 Myr ago as evidenced by U–Pb dating on calcite in fault zone cataclasite, *Solid Earth*, **12**(1), 237–251.

Bodin, T., Sambridge, M., Rawlinson, N., & Arroucau, P., 2012. Transdimensional tomography with unknown data noise, *Geophysical Journal International*, **189**(3), 1536–1556.

Boué, P., Roux, P., Campillo, M., & Briand, X., 2014. Phase velocity tomography of surface waves using ambient noise cross correlation and array processing, *Journal of Geophysical Research: Solid Earth*, **119**(1), 519–529.

Brocher, T., 2005. Empirical Relations between Elastic Wavespeeds and Density in the Earth's Crust, *Bulletin of the Seismological Society of America*, **95**, 2081–2092.

Burov, E., Francois, T., Yamato, P., & Wolf, S., 2014. Mechanisms of continental subduction and exhumation of HP and UHP rocks, *Gondwana Research*, **25**(2), 464–493.

Campillo, M. & Paul, A., 2003. Long-Range Correlations in the Diffuse Seismic Coda, *Science*, **299**(5606), 547–549.

Chopin, C., 1984. Coesite and pure pyrope in high-grade blueschists of the Western Alps: a first record and some consequences, *Contributions to Mineralogy and Petrology*, **86**(2), 107–118.

Closs, H. & Labrouste, Y., 1963. Recherches séismologiques dans les alpes occidentales au moyen des grandes explosions en 1956, 1958 et 1960: Année géophysique internationale, *CNRS, 12e série, fasc. II*.

Crawford, W. & Webb, S., 2000. Identifying and Removing Tilt Noise from Low-Frequency (<0.1 Hz) Seafloor Vertical Seismic Data, *Bulletin of the Seismological Society of America*, **90**, 952–963.

Deen, M., Wielandt, E., Stutzmann, E., Crawford, W., Barruol, G., & Sigloch, K., 2017. First Observation of the Earth's Permanent Free Oscillations on Ocean Bottom Seismometers, *Geophysical Research Letters*, **44**(21), 10,988–10,996.

Diehl, T., Husen, S., Kissling, E., & Deichmann, N., 2009. High-resolution 3-D P-wave model of the Alpine crust, *Geophysical Journal International*, **179**(2), 1133–1147.

Duchêne, S., Blichert-Toft, J., Luais, B., Télouk, P., Lardeaux, J.-M., & Albarede, F., 1997. The Lu–Hf dating of garnets and the ages of the alpine high-pressure metamorphism, *Nature*, **387**(6633), 586–589.

Dumont, T., Schwartz, S., Guillot, S., Simon-Labric, T., Tricart, P., & Jourdan, S., 2012. Structural and sedimentary records of the Oligocene revolution in the Western Alpine arc, *Journal of Geodynamics*, **56-57**, 18–38, Geodynamics and Orogenesis.

Dziewonski, A., Bloch, S., & Landisman, M., 1969. A technique for the analysis of transient seismic signals, *Bulletin of the Seismological Society of America*, **59**(1), 427–444.

Dziewonski, A. M. & Anderson, D. L., 1981. Preliminary reference Earth model, *Physics of the Earth and Planetary Interiors*, **25**(4), 297 – 356.

Eva, E., Malusà, M. G., & Solarino, S., 2015. A seismotectonic picture of the inner southern Western Alps based on the analysis of anomalously deep earthquakes, *Tectonophysics*, **661**, 190–199.

Eva, E., Malusà, M. G., & Solarino, S., 2020. Seismotectonics at the Transition Between Opposite-Dipping Slabs (Western Alpine Region), *Tectonics*, **39**(9), e2020TC006086.

Faccenna, C., Becker, T. W., Auer, L., Billi, A., Boschi, L., Brun, J. P., Capitanio, F. A., Funiciello, F., Horvàth, F., Jolivet, L., Piromallo, C., Royden, L., Rossetti, F., & Serpelloni, E., 2014. Mantle dynamics in the Mediterranean, *Reviews of Geophysics*, **52**(3), 283–332.

Federal Institute for Geosciences & Natural Resources (BGR), 1976. German Regional Seismic Network (GRSN), Publisher: Federal Institute for Geosciences and Natural Resources (BGR).

Ford, Lickorish, & Kusznir, 1999. Tertiary foreland sedimentation in the Southern Subalpine Chains, SE France: a geodynamic appraisal, *Basin Research*, **11**, 315–336.

Galetti, E., Curtis, A., Meles, G. A., & Baptie, B., 2015. Uncertainty Loops in Travel-Time Tomography from Nonlinear Wave Physics, *Phys. Rev. Lett.*, **114**, 148501.

GEOFON Data Centre, 1993. GEOFON seismic network, Publisher: Deutsches GeoForschungsZentrum GFZ.

Guillot, S., Hattori, K., Agard, P., Schwartz, S., & Vidal, O., 2009. Exhumation Processes in Oceanic and Continental Subduction Contexts: A Review, in Subduction Zone Geodynamics, pp. 175–205, Springer Berlin Heidelberg, Berlin, Heidelberg.

Handy, M., Schmid, S., Bousquet, R., Kissling, E., & Bernoulli, D., 2010. Reconciling plate-tectonic reconstructions of Alpine Tethys with the geological-geophysical record of spreading and subduction in the Alps, *Earth-Science Reviews*, **102**, 121–158.

Herrmann, R. B., 1973. Some aspects of band-pass filtering of surface waves, *Bulletin of the Seismological Society of America*, **63**(2), 663–671.

Herrmann, R. B., 2013. Computer Programs in Seismology: An Evolving Tool for Instruction and Research, *Seismological Research Letters*, **84**(6), 1081–1088.

Hetényi, G., Molinari, I., & Clinton, J., 2018. The AlpArray Seismic Network: A Large-Scale European Experiment to Image the Alpine Orogen, *Surveys in Geophysics*, **39**.

Hetényi, G., Plomerová, J., Bianchi, I., Kampfová Exnerová, H., Bokelmann, G., Handy, M. R., & Babuška, V., 2018. From mountain summits to roots: Crustal structure of the eastern alps and bohemian massif along longitude 13.3°E, *Tectonophysics*, **744**, 239–255.

Hirn, A., Nadir, S., Thouvenot, F., Nicolich, R., Pellis, G., Scarascia, S., Tabacco, I., Castellano, M., & Merlantip, F., 1989. A new picture of the Moho under the western Alps, *Nature*, **337**, 249–251.

INGV Seismological Data Centre, 2006. Rete Sismica Nazionale (RSN), Publisher: Istituto Nazionale di Geofisica e Vulcanologia (INGV), Italy.

Institut Cartogràfic I Geològic De Catalunya - Institut D'Estudis Catalans, 1984. Catalan Seismic Network, Publisher: International Federation of Digital Seismograph Networks.

Institut de Physique du Globe de Paris (IPGP) & Ecole et Observatoire des Sciences de la Terre de Strasbourg (EOST), 1982. GEOSCOPE, French Global Network of broad band seismic stations, Publisher: Institut de Physique du Globe de Paris (IPGP).

Institute Of Geophysics Of The Academy Of Sciences Of The Czech Republic , 1973. Czech Regional Seismic Network, Publisher: International Federation of Digital Seismograph Networks.

Instituto Geografico Nacional, Spain, 1999. Spanish Digital Seismic Network, Publisher: International Federation of Digital Seismograph Networks.

Jourdon, A., Rolland, Y., Petit, C., & Bellahsen, N., 2014. Style of Alpine tectonic deformation in the Castellane fold-and-thrust belt (SW Alps, France): Insights from balanced cross-sections, *Tectonophysics*, **633**, 143–155.

KNMI, 1993. Netherlands Seismic and Acoustic Network, Publisher: Royal Netherlands Meteorological Institute (KNMI).

Kästle, E. D., El-Sharkawy, A., Boschi, L., Meier, T., Rosenberg, C., Bellahsen, N., Cristiano, L., & Weidle, C., 2018. Surface Wave Tomography of the Alps Using Ambient-Noise and Earthquake Phase Velocity Measurements, *Journal of Geophysical Research: Solid Earth*, **123**(2), 1770–1792.

Lardeaux, J.-M., Schwartz, S., Tricart, P., Paul, A., Guillot, S., Béthoux, N., & Masson, F., 2006. A crustal-scale cross-section of the south-western Alps combining geophysical and geological imagery, *Terra Nova*, **18**, 412–422.

Levshin, A., Yanovskaya, T., Lander, A., Bukchin, B., Barmin, M., Its, E., & Ratnikova, L., 1989. *Seismic Surface Waves in a Laterally Inhomogeneous Earth*, Kluwer Publ, Dordrecht, pp 129–182.

Liao, J., Malusà, M. G., Zhao, L., Baldwin, S. L., Fitzgerald, P. G., & Gerya, T., 2018. Divergent plate motion drives rapid exhumation of (ultra)high pressure rocks, *Earth and Planetary Science Letters*, **491**, 67–80.

Liu, D., Zhao, L., Paul, A., Yuan, H., Solarino, S., Aubert, C., Pondrelli, S., Salimbeni, S., Eva, E., Malusà, M. G., & Guillot, S., 2022. Receiver function mapping of the mantle transition zone

beneath the western alps: New constraints on slab subduction and mantle upwelling, *Earth and Planetary Science Letters*, **577**, 117267.

Lu, Y., Stehly, L., Paul, A., & AlpArray Working Group, 2018. High-resolution surface wave tomography of the European crust and uppermost mantle from ambient seismic noise, *Geophysical Journal International*, **214**(2), 1136–1150.

Lu, Y., Stehly, L., Brossier, R., Paul, A., & AlpArray Working Group, 2020. Imaging Alpine crust using ambient noise wave-equation tomography, *Geophysical Journal International*, **222**(1), 69–85.

Macquet, M., Paul, A., Pedersen, H. A., Villaseñor, A., Chevrot, S., Sylvander, M., Wolyniec, D., & Pyrope Working Group, 2014. Ambient noise tomography of the Pyrenees and the surrounding regions: inversion for a 3-D Vs model in the presence of a very heterogeneous crust, *Geophysical Journal International*, **199**(1), 402–415.

Malinverno, A. & Briggs, V., 2004. Expanded uncertainty quantification in inverse problems: Hierarchical Bayes and empirical Bayes, *Geophysics*, **69**, 1005–1016.

Malusà, M., Guillot, S., Zhao, L., Paul, A., Solarino, S., Dumont, T., Schwartz, S., Aubert, C., Baccheschi, P., Eva, E., Lu, Y., Lyu, C., Agostinetti, N., Pondrelli, S., Salimbeni, S., Sun, W., & Yuan, H., 2021. The Deep Structure of the Alps based on the CIFALPS Seismic Experiment: A Synthesis, *Geochemistry, Geophysics, Geosystems*.

Malusà, M. G., Zhao, L., Eva, E., Solarino, S., Paul, A., Guillot, S., Schwartz, S., Dumont, T., Aubert, C., Salimbeni, S., Pondrelli, S., Wang, Q., & Zhu, R., 2017. Earthquakes in the western Alpine mantle wedge, *Gondwana Research*, **44**, 89–95.

Mathey, M., Sue, C., Pagani, C., Baize, S., Walpersdorf, A., Bodin, T., Husson, L., Hannouz, E., & Potin, B., 2020. Present-day geodynamics of the Western Alps: new insights from earthquake mechanisms, *Solid Earth Discussions*, **2020**, 1–38.

Molinari, I., Verbeke, J., Boschi, L., Kissling, E., & Morelli, A., 2015. Italian and Alpine three-dimensional crustal structure imaged by ambient-noise surface-wave dispersion, *Geochemistry, Geophysics, Geosystems*, **16**(12), 4405–4421.

Mosca, P., Riccardo, P., Rogledi, S., & Rossi, M., 2010. New data for the kinematic interpretation of the Alps–Apennines junction (Northwestern Italy), *International Journal of Earth Sciences*, **99**, 833–849.

Nicolas, A., Hirn, A., Nicolich, R., & Polino, R., 1990. Lithospheric wedging in the western Alps inferred from the ECORS-CROP traverse, *Geology*, **18**(7), 587–590.

Paul, A., Cattaneo, M., Thouvenot, F., Spallarossa, D., Béthoux, N., & Fréchet, J., 2001. A three-dimensional crustal velocity model of the southwestern Alps from local earthquake tomography, *Journal of Geophysical Research: Solid Earth*, **106**(B9), 19367–19389.

Polino, R., Piaz, G. D., & Gosso, G., 1990. Tectonic erosion at the Adria Margin and accrertionary processes for the Cretaceous orogeny of the Alps.

Rawlinson, N. & Sambridge, M., 2004. Wave front evolution in strongly heterogeneous layered media using the fast marching method, *Geophysical Journal International*, **156**(3), 631–647.

RESIF, 1995. RESIF-RLBP French Broad-band network, RESIF-RAP strong motion network and other seismic stations in metropolitan France, Publisher: RESIF - Réseau Sismologique et géodésique Français.

Royal Observatory Of Belgium, 1985. Belgian Seismic Network, Publisher: International Federation of Digital Seismograph Networks.

Schmid, S. M., Kissling, E., Diehl, T., van Hinsbergen, D. J., & Molli, G., 2017. Ivrea mantle wedge, arc of the Western Alps, and kinematic evolution of the Alps–Apennines orogenic system, *Swiss Journal of Geosciences*, **110**(2), 581–612.

Schwartz, S., Allemand, P., & Guillot, S., 2001. Numerical model of the effect of serpentinites on the exhumation of eclogitic rocks: insights from the Monviso ophiolitic massif (Western Alps), *Tectonophysics*, **342**(1), 193–206.

Schwartz, S., Tricart, P., Lardeaux, J.-M., Guillot, S., & Vidal, O., 2009. Late tectonic and metamorphic evolution of the Piedmont accretionary wedge (Queyras Schistes lustrés, Western Alps): Evidences for tilting during Alpine collision, *Geological Society of America Bulletin*, **121**(3-4), 502–518.

Schwartz, S., Gautheron, C., Audin, L., Dumont, T., Nomade, J., Barbarand, J., Pinna Jamme, R., & van der Beek, P., 2017. Foreland exhumation controlled by crustal thickening in the Western Alps, *Geology*, **45**, 139–142.

Shapiro, N., Campillo, M., Stehly, L., & Ritwoller, M., 2005. High-resolution surface-wave tomography from ambient seismic noise., *Science*, **307 (5715)**, 1615–1618.

Shapiro, N. M. & Campillo, M., 2004. Emergence of broadband Rayleigh waves from correlations of the ambient seismic noise, *Geophysical Research Letters*, **31**(7).

Shapiro, N. M. & Singh, S. K., 1999. A systematic error in estimating surface-wave group-velocity dispersion curves and a procedure for its correction, *Bulletin of the Seismological Society of America*, **89**(4), 1138–1142.

Simon-Labric, T., Rolland, Y., Dumont, T., Heymes, T., Authemayou, C., Corsini, M., & Fornari, M., 2009. 40Ar/ 39Ar dating of Penninic Front tectonic displacement (W Alps) during the Lower Oligocene (31–34 Ma), *Terra Nova*, **21**(2), 127–136.

Slovenian Environment Agency, 2001. Seismic Network of the Republic of Slovenia, Publisher: International Federation of Digital Seismograph Networks.

SNSN, 1904. Swedish National Seismic Network, Publisher: Uppsala University, Uppsala, Sweden.

Soergel, D., Pedersen, H. A., Stehly, L., Margerin, L., Paul, A., & AlpArray Working Group, 2019. Coda-Q in the 2.5–20 s period band from seismic noise: application to the greater Alpine area, *Geophysical Journal International*, **220**(1), 202–217.

Solarino, S., Malusà, M. G., Eva, E., Guillot, S., Paul, A., Schwartz, S., Zhao, L., Aubert, C., Dumont, T., Pondrelli, S., Salimbeni, S., Wang, Q., Xu, X., Zheng, T., & Zhu, R., 2018. Mantle wedge exhumation beneath the Dora-Maira (U)HP dome unravelled by local earthquake tomography (Western Alps), *Lithos*, **296-299**, 623 – 636.

Spada, M., Bianchi, I., Kissling, E., Agostinetti, N. P., & Wiemer, S., 2013. Combining controlled-source seismology and receiver function information to derive 3-D Moho topography for Italy, *Geophysical Journal International*, **194**(2), 1050–1068.

Stehly, L., Campillo, M., Froment, B., & Weaver, R. L., 2008. Reconstructing Green's function by correlation of the coda of the correlation (C3) of ambient seismic noise, *Journal of Geophysical Research: Solid Earth*, **113**(B11).

Stehly, L., Fry, B., Campillo, M., Shapiro, N. M., Guilbert, J., Boschi, L., & Giardini, D., 2009. Tomography of the Alpine region from observations of seismic ambient noise, *Geophysical Journal International*, **178**(1), 338–350.

Swiss Seismological Service (SED) At ETH Zurich, 1983. National Seismic Networks of Switzerland, Publisher: ETH Zürich.

Thouvenot, F., Paul, A., Fréchet, J., Béthoux, N., Jenatton, L., & Guiguet, R., 2007. Are there really superposed Mohos in the southwestern Alps? New seismic data from fan-profiling reflections, *Geophysical Journal International*, **170**(3), 1180–1194.

University Of Zagreb, 2001. Croatian Seismograph Network, Publisher: International Federation of Digital Seismograph Networks.

Verbeke, J., Boschi, L., Stehly, L., Kissling, E., & Michelini, A., 2012. High-resolution Rayleigh-wave velocity maps of central Europe from a dense ambient-noise data set, *Geophysical Journal International*, **188**(3), 1173–1187.

Vinnik, L., 1977. Detection of waves converted from P to SV in the mantle, *Physics of the Earth and Planetary Interiors*, **15**(1), 39–45.

Zahorec, P., Papčo, J., Pašteka, R., Bielik, M., Bonvalot, S., Braitenberg, C., Ebbing, J., Gabriel, G., Gosar, A., Grand, A., et al., 2021. The first pan-alpine surface-gravity database, a modern compilation that crosses frontiers, *Earth System Science Data*, **13**(5), 2165–2209.

ZAMG-Zentralanstalt Für Meterologie Und Geodynamik, 1987. Austrian Seismic Network, Publisher: International Federation of Digital Seismograph Networks.

Zhao, L., Paul, A., Guillot, S., Solarino, S., Malusà, M., Zheng, T., Salimbeni, S., Dumont, T., Schwartz, S., Zhu, R., & Wang, Q., 2015. First Seismic Evidence for Continental Subduction beneath the Western Alps, *Geology*, **43**, 815–818.

Zhao, L., Paul, A., Solarino, S., & RESIF, 2016. Seismic network YP: CIFALPS temporary experiment (China-Italy-France Alps seismic transect).

Zhao, L., Paul, A., Solarino, S., & RESIF, 2018. Seismic network XT: CIFALPS temporary experiment (China-Italy-France Alps seismic transect).

Zhao, L., Malusà, M. G., Yuan, H., Paul, A., Guillot, S., Lu, Y., Stehly, L., Solarino, S., Eva, E., Lu, G., & Bodin, T., 2020. Evidence for a serpentinized plate interface favouring continental subduction, *Nature Communications*, **11**, 2171.

Zhu, L., 2000. Crustal structure across the San Andreas Fault, southern California from teleseismic converted waves, *Earth and Planetary Science Letters*, **179**(1), 183–190.

Ziegler, P. A., 1992. European Cenozoic rift system, *Tectonophysics*, **208**(1), 91–111.

Supplementary material

Lithospheric transdimensional ambient noise tomography of W-Europe: implications for crustal scale geometry of the W-Alps

A. Nouibat[1], L. Stehly[1], A. Paul[1], S. Schwartz[1], T. Bodin[2], T. Dumont[1], Y. Rolland[1,3], R. Brossier[1], Cifalps Team and AlpArray Working Group

[1] Univ. Grenoble Alpes, Univ. Savoie Mont Blanc, CNRS, IRD, UGE, ISTerre, *38000 Grenoble, France.*

[2] Univ. Lyon, UCBL, CNRS, LGL-TPE, *69622 Villeurbanne, France.*

[3] Univ. Savoie Mont Blanc, CNRS, UMR 5204, EDYTEM, *73370 Le Bourget-du-Lac, France.*

1 Distance-time plot of noise correlations

Fig. S1 shows a distance-time section of vertical-component seismic ambient noise cross-correlations computed in a region including most of the Western Alps. The dispersive Rayleigh wave emerges very clearly with a fairly good symmetry between the causal and acausal parts.

2 Comparison of the 8-s and 25-s group-velocity maps with sedimentary basins and Moho depth maps

Figure S2(a) shows the 8-s group-velocity map together with main sedimentary basins. Figure S2(b) shows the 25-s group-velocity map with contours of the reference Moho depth model of Spada et al. (2013), that is mainly derived from controlled-source seismology (CSS) and receiver-function data. The thick crust of the Alps and the Apennines mountain belts coincides with areas of low velocity < 3.0 km/s. Areas of thin crust such as the Liguro-Provençal basin and the Tyrrhenian Sea coincide with high velocity anomalies > 3.4 km/s .

3 Comparison with a matrix-based inversion

We compared results of the *rj-McMC* algorithm with a matrix-based linearized inversion (Boschi & Dziewonski., 1999) for the same dataset at 15 s period (Fig. S3). The linear problem is solved using an iterative *LSQR* algorithm (Paige and Saunders., 1982). The model solution is computed using an adaptive grid-based path density that remains fixed during inversion (Schaefer et al., 2011; Lu et al., 2018; Fig. S3(a)). Cell sizes of 0.15°, 0.3° and 0.6° were used depending on the path density (Fig. S3(b)). The regularization coefficients (damping, roughness) were set according to the maximum curvature of the *L-curve*. Fig. S3(c) shows the *rj-McMC* solution model computed by averaging the ensemble of models obtained from 64 Markov chains in parallel after 180×10^3 steps. The posterior map of velocity uncertainties is generated by computing the variance of this ensemble (Fig. S3(d)). The image resulting from the *rj-McMC* inversion is not as smooth as the one resulting from the linearized inversion, which is affected by the imposed degree of smoothing. On the other hand, a stronger velocity contrast is obtained using the trans-D inversion, with more focused anomalies that suggest a better resolution (see for example the low-velocity anomaly in the Po plain). In addition, the trans-D inversion highlights new features such as the high-velocity anomaly at 4° longitude and 43.5° latitude.

4 Posterior distribution on the number of Voronoi cells

Figure S4 shows the posterior probability distribution on the number of Voronoi cells used to describe the 2-D velocity field in the *rj-McMC* tomography shown in Fig. S3(c). The small standard deviation of the Gaussian-shaped probability density curve shows that the algorithm has converged. The maximum model solution occurs for $760 - 770$ Voronoi cells.

5 Inversion misfit

Figure S5(a) shows the evolution of the normalized model misfit function with the number of iterations in the *rj-McMC* inversion shown in Fig. S3(c). The misfit reduction reaches $\sim 90\%$. The posterior histogram of traveltime misfit between model predictions and observations is shown in Fig. S5(b).

6 Checkerboard tests

In Fig. S6, we check the resolution power of the *rj-McMC* inversion by synthetic checkerboard tests for cell sizes of 1° and 2°. Figures S6(1a)-(2a) show input models with square-shaped anomalies. Synthetic travel times were computed using the same source and receiver geometry as in observations at 15 s period, with added random Gaussian noise of 1 s standard deviation. Figures S6(1b)-(2b) show the average solution models obtained from the *rj-McMC* tomography. The Hierarchical Bayes reversible jump method is able to recover the velocity areas as defined in the synthetic models.

7 Depth sections through the V_s model along reference profiles

In Fig. S7, we present depth sections along three reference profiles across the Alpine mountain range: Cifalps and ECORS-CROP in the Western Alps and the alpine part of the EASI N-S transect in the Eastern Alps.

8 Comparison with the V_s model by Zhao et al. (2020)

Fig. S8 shows a comparison between our V_s model and the one by Zhao et al. (2020) on depth sections along the Cifalps and ECORS-CROP profiles. To facilitate the comparison between the results of the two models, we added on each depth section the reference Moho depth model of Spada et al. (2013) and the 4.3 km/s iso-velocity contour that we use as a proxy for the Moho (see discussion in section 5.2 of the main text). The middle and lower crust of the western parts of both profiles have higher velocities in our model than in Zhao et al. (2020). This difference is most probably due to the improved data coverage in our dataset with respect to the one of Lu et al. (2018) used in the inversion of Zhao et al. (2020), in particular in the westernmost part of the AlpArray network. In the alpine part of the Cifalps section, the model by Zhao et al. (2020) and our model exhibit similar first order features. In particular, they exhibit consistent geometries of the Ivrea body and similar Moho depths.

By contrast, these two models exhibit striking differences along the ECORS-CROP transect. The depth of the 4.3 km/s iso-velocity in our model is consistent with the Moho depth of Spada et al. (2013), but is deeper in Zhao et al. (2020). The 3.8 km/s V_s contour would better fit the Moho model of Spada et al. (2013), although 3.8 km/s is rather low for a Moho proxy.

Another striking difference is the velocity gradient at the Moho, which is strong in our model and smooth in Zhao et al. (2020). Our strong gradient is more in line with the results of receiver functions studies (Zhao et al., 2015) and seismic reflection profiling (e.g. ECORS-CROP Deep Seismic Sounding Group, 1989; Thouvenot et al., 2007) in the Western Alps, which documented a highly reflective Moho. This strong velocity gradient at Moho depth in our model is a direct consequence of the chosen parameterization and the 4-layer model assumption. By contrast, the reference model in the transdimensional inversion of Zhao et al. (2020) is a homogeneous half-space of 3.8 km/s velocity.

References

Boschi, L. and Dziewonski, A. M. (1999). High- and low-resolution images of the Earth's mantle: Implications of different approaches to tomographic modeling. *Journal of Geophysical Research: Solid Earth*, 104(B11):25567–25594.

Hetényi, G., Plomerová, J., Bianchi, I., Kampfová Exnerová, H., Bokelmann, G., Handy, M. R., and Babuška, V. (2018). From mountain summits to roots: Crustal structure of the eastern alps and bohemian massif along longitude 13.3°e. *Tectonophysics*, 744:239–255.

Hirn, A., Nadir, S., Thouvenot, F., Nicolich, R., Pellis, G., Scarascia, S., Tabacco, I., Castellano, M., and Merlantip, F. (1989). A new picture of the Moho under the western Alps. *Nature*, 337:249–251.

Lu, Y., Stehly, L., Paul, A., and AlpArray Working Group (2018). High-resolution surface wave tomography of the European crust and uppermost mantle from ambient seismic noise. *Geophysical Journal International*, 214(2):1136–1150.

Paige, C. C. and Saunders, M. A. (1982). LSQR: An Algorithm for Sparse Linear Equations and Sparse Least Squares. *ACM Trans. Math. Softw.*, 8(1):43–71.

Schaefer, J. F., Boschi, L., and Kissling, E. (2011). Adaptively parametrized surface wave tomography: methodology and a new model of the European upper mantle. *Geophysical Journal International*, 186(3):1431–1453.

Spada, M., Bianchi, I., Kissling, E., Agostinetti, N. P., and Wiemer, S. (2013). Combining controlled-source seismology and receiver function information to derive 3-D Moho topography for Italy. *Geophysical Journal International*, 194(2):1050–1068.

Thouvenot, F., Paul, A., Fréchet, J., Béthoux, N., Jenatton, L., and Guiguet, R. (2007). Are there really superposed Mohos in the southwestern Alps? New seismic data from fan-profiling reflections. *Geophysical Journal International*, 170(3):1180–1194.

Zhao, L., Malusà, M. G., Yuan, H., Paul, A., Guillot, S., Lu, Y., Stehly, L., Solarino, S., Eva, E., Lu, G., and Bodin, T. (2020). Evidence for a serpentinized plate interface favouring continental subduction. *Nature Communications*, 11:2171.

Zhao, L., Paul, A., Guillot, S., Solarino, S., Malusà, M., Zheng, T., Salimbeni, S., Dumont, T., Schwartz, S., Zhu, R., and Wang, Q. (2015). First Seismic Evidence for Continental Subduction beneath the Western Alps. *Geology*, 43:815–818.

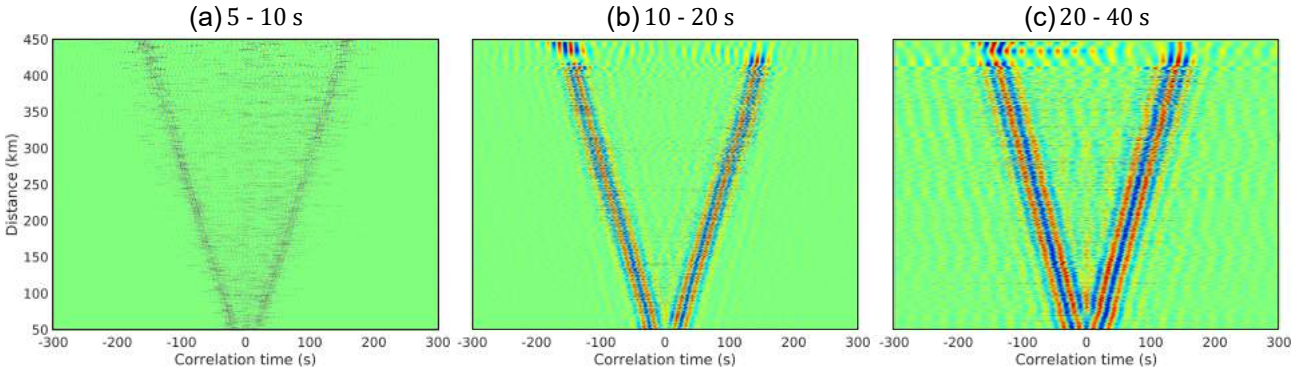

Figure S1. Sections of noise cross-correlation traces in the $5-10$ s, $10-20$ s and $20-40$ s period bands. The trace amplitudes are normalized to one. The causal part (positive times) corresponds to Rayleigh waves propagating eastwards while the acausal part (negative times) corresponds to Rayleigh waves propagating westwards.

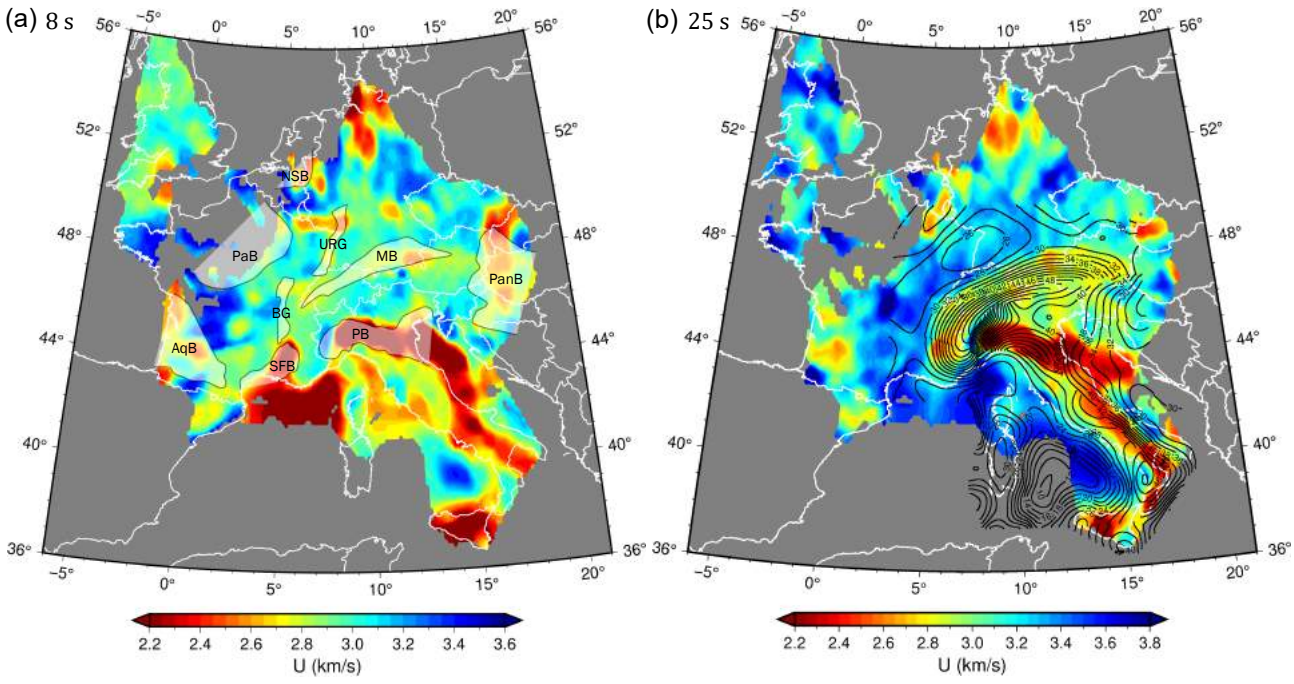

Figure S2. (a) Group-velocity map at 8 s period and Jurassic to Tertiary main sedimentary basins (shown as partially transparent areas). NSB: North-Sea basin, PB: Po basin, SFB: Southeast-France basin, AqB: Aquitaine basin, PaB: Paris basin, BG: Bresse Graben, URG: Upper Rhine Graben, MB: Molasse basin, PanB: Pannonian Basin. (b) Group-velocity map at 25 s period. Black lines are contours of the reference Moho depth map by Spada et al. (2013).

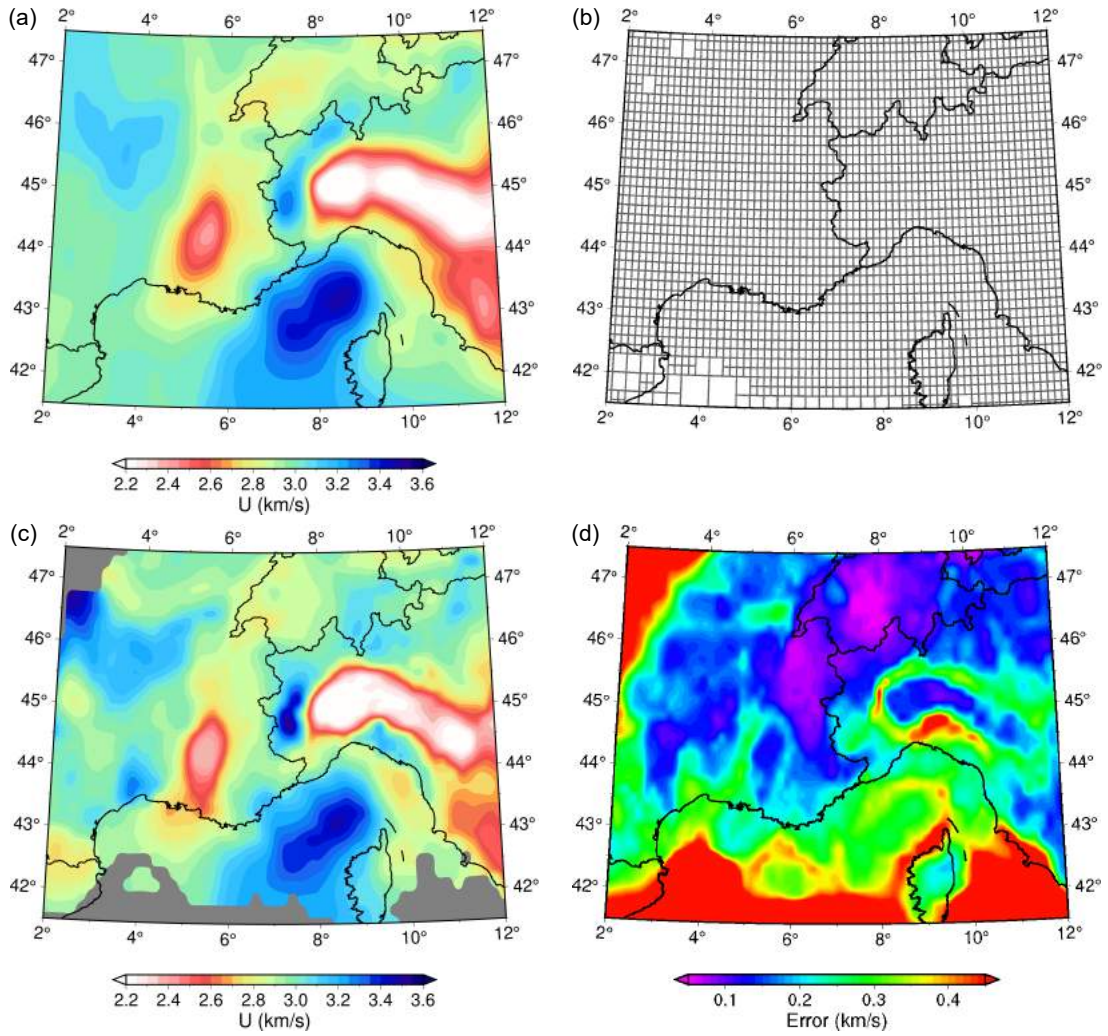

Figure S3. Comparison of the result of our Hierarchical Bayes inversion with the result of a matrix-based inversion at 15 *s* period. (a) Group-velocity map output of the regularized method. (b) Adaptive grid used to produce the regularized solution model. (c) Result of the Hierarchical Bayes reversible jump method. (d) Estimated error for the reversible jump tomography.

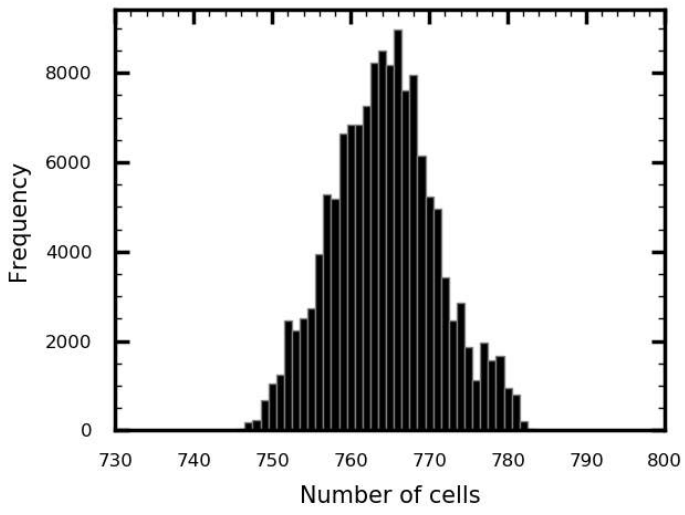

Figure S4. Posterior probability density for the number of Voronoi cells at 15 *s* period.

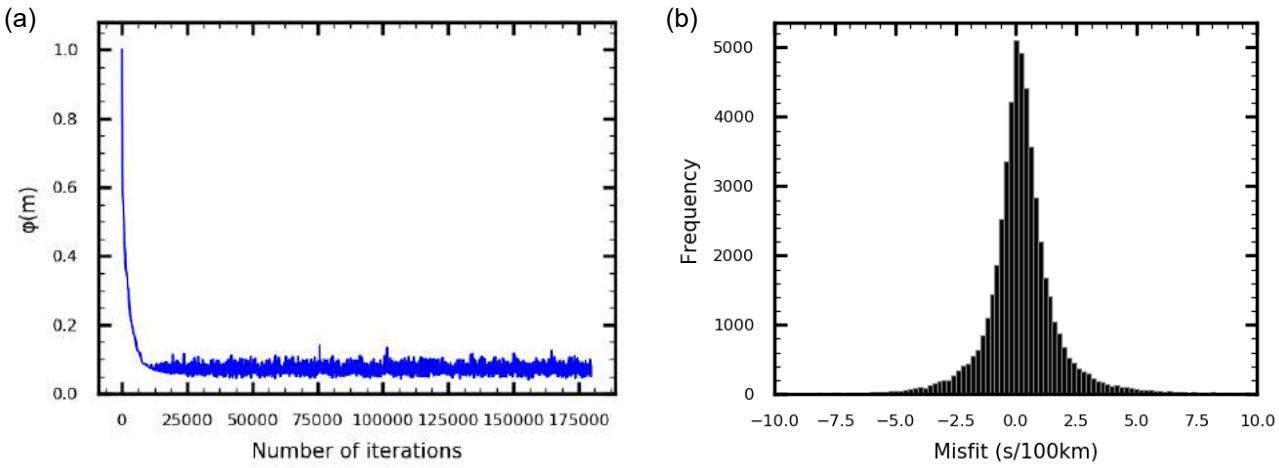

Figure S5. Misfit outputs at 15 *s* period from the reversible jump tomography. (a) Model misfit variation as a function of the number of iterations. (b) Histogram of traveltime misfit.

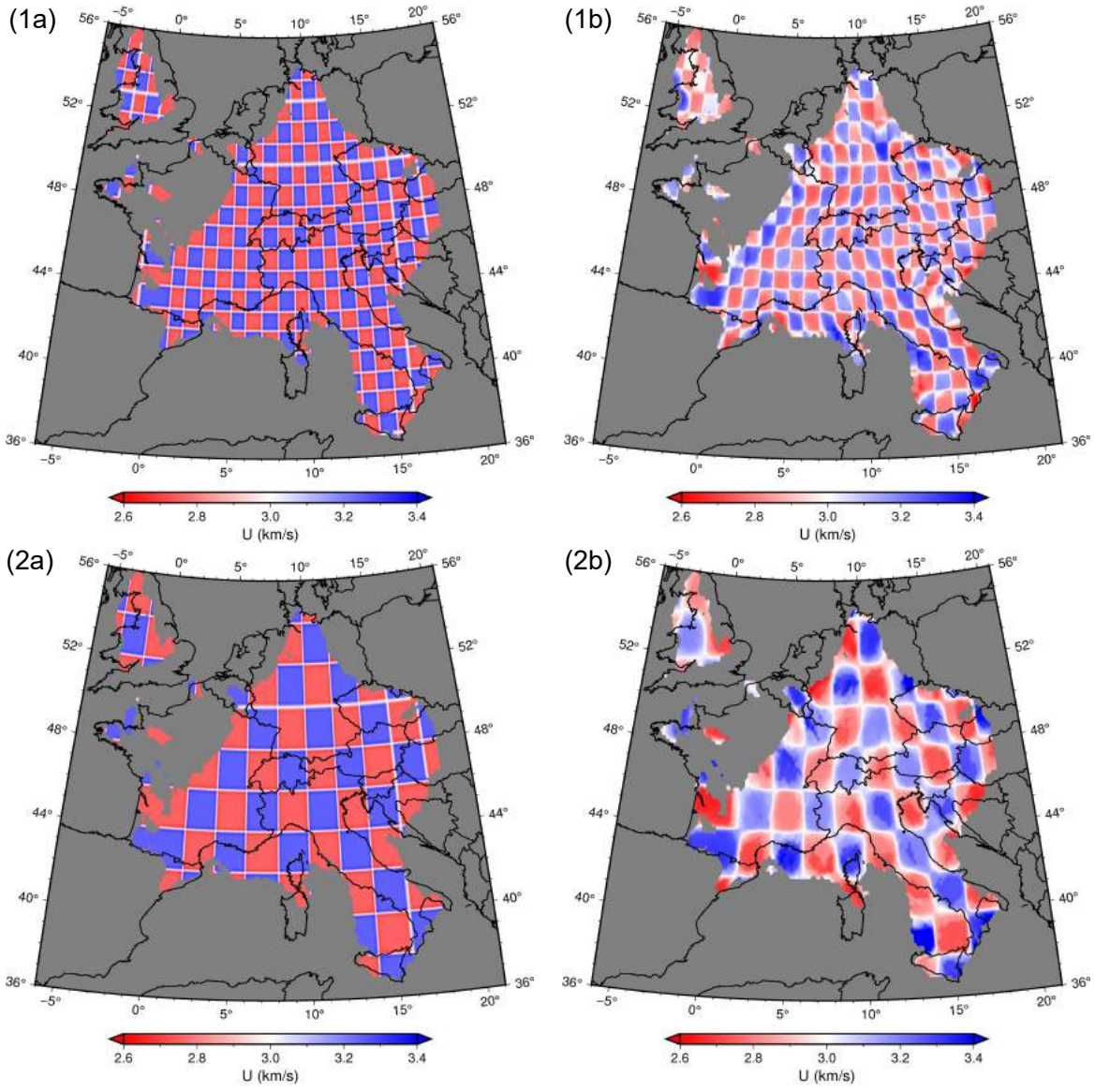

Figure S6. (1a) Input synthetic velocity model with a cell size of 1°. (1b) Average solution model of the Hierarchical Bayes reversible jump tomography. (2a) Input synthetic velocity model with a cell size of 2°. (2b) Average solution model of the Hierarchical Bayes reversible jump tomography.

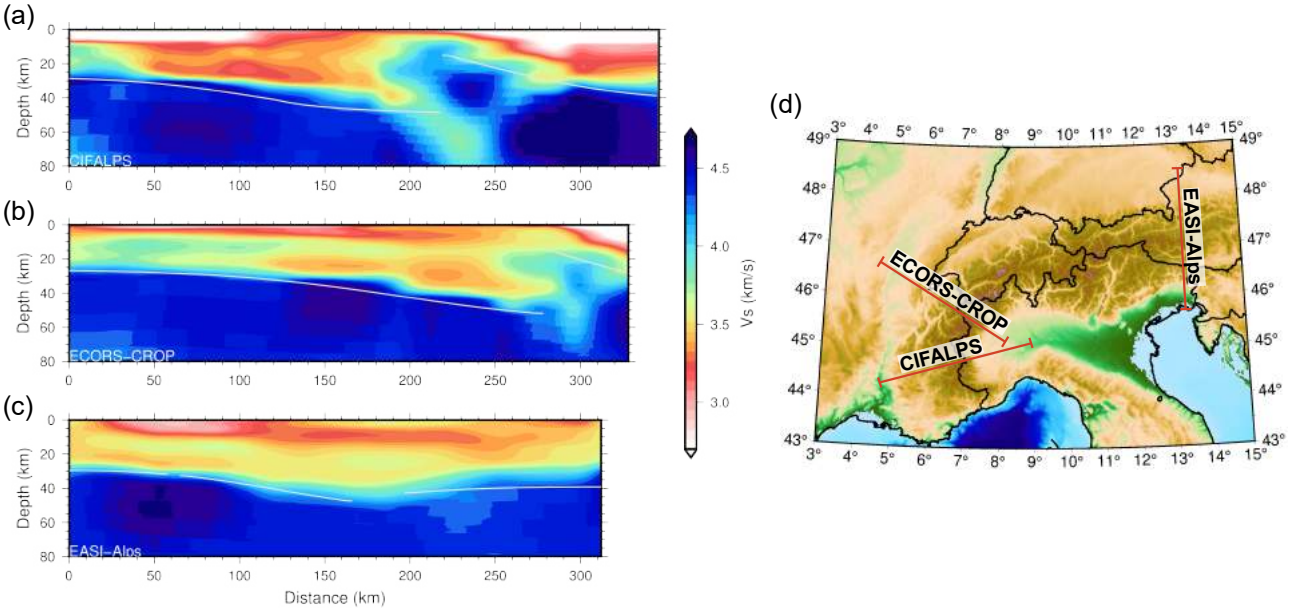

Figure S7. Cross sections in our V_s model along: a) the CIFALPS profile, b) the ECORS-CROP profile, and c) the alpine part of the EASI profile (Hetényi et al., 2018). The white lines show Spada et al. (2013)'s Moho depth model. (d) Location map of the three profiles.

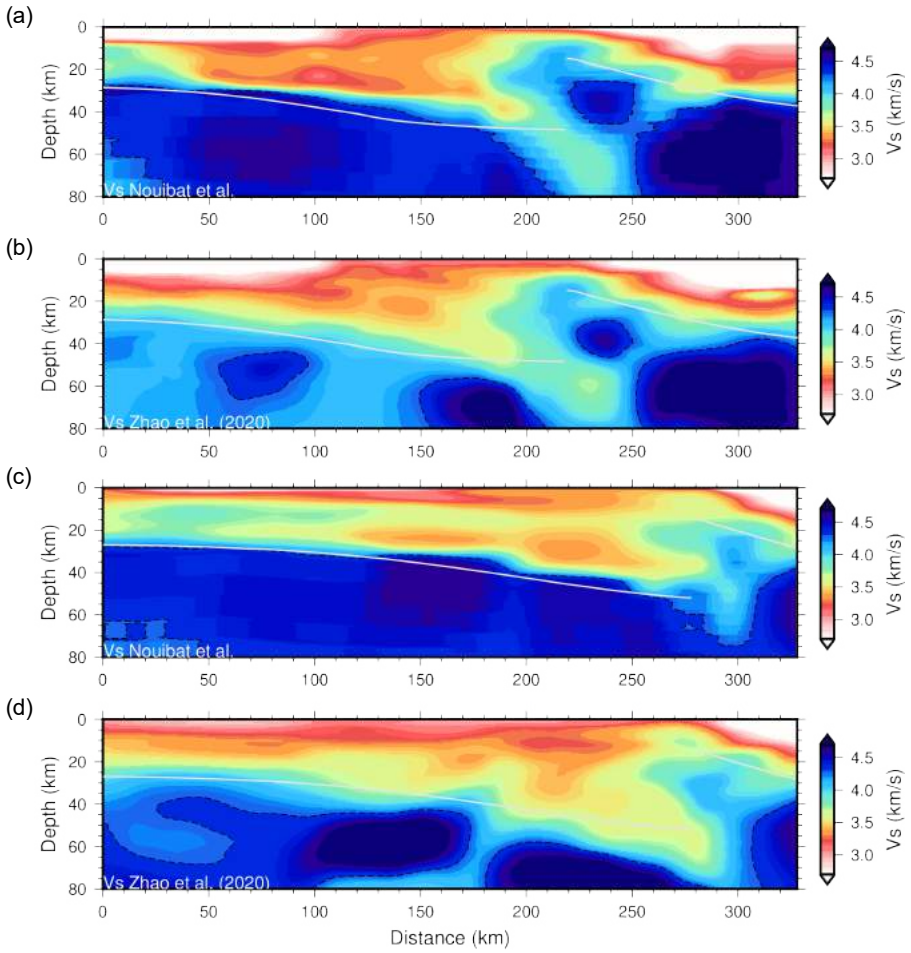

Figure S8. Cross sections in our V_s model and in the V_s model of Zhao et al. (2020), along the Cifalps (a, b) and ECORS-CROP (c, d) profiles. The dashed black lines correspond to the 4.3 km/s velocity contour. The thick white lines correspond to Spada et al. (2013)'s Moho depth.